Homeostatic Plasticity Commonly Fails at the Intersection of Autism-Gene Mutations and a Novel Class of Common Phenotypic Modifier

Özgür Genç[1], Joon Y. An[2], Richard D. Fetter[1], Yelena Kulik[1], Giulia Zunino[1], Stephan J. Sanders[2] and Graeme W. Davis[1]*

1. Department of Biochemistry and Biophysics
Kavli Institute for Fundamental Neuroscience
University of California, San Francisco
San Francisco, CA 94158

2. Department of Psychiatry
UCSF Weill Institute for Neurosciences
University of California, San Francisco
San Francisco, CA 94158

*to whom correspondence should be addressed
Graeme.davis@ucsf.edu

ABSTRACT

We identify a set of common phenotypic modifiers that interact with five independent autism gene orthologs (*RIMS1*, *CHD8*, *CHD2*, *WDFY3*, *ASH1L*) causing a common failure of presynaptic homeostatic plasticity (PHP). Heterozygous null mutations in each autism gene are demonstrated to have normal baseline neurotransmission and PHP. However, we find that PHP is sensitized and rendered prone to failure. A subsequent electrophysiology-based genetic screen identifies the first known heterozygous mutations that commonly genetically interact with multiple ASD gene orthologs, causing PHP to fail. Two phenotypic modifiers identified in the screen, *PDPK1* and *PPP2R5D,* are characterized. Finally, transcriptomic, ultrastructural and electrophysiological analyses define one mechanism by which PHP fails; an unexpected, maladaptive up-regulation of *CREG*, a conserved, neuronally expressed, stress response gene and a novel repressor of PHP. Thus, we define a novel genetic landscape by which diverse, unrelated autism risk genes may converge to commonly affect the robustness of synaptic transmission.

Keywords: Presynaptic homeostatic plasticity; PHP; synaptic homeostasis; homeostatic plasticity; autism spectrum disorder; ASD; synaptic transmission; chromatin remodeling; Rim; RIMS1; PDPK1; PPP2R5D; functional genomics; CREG; intellectual disability; CHD8; ASH1L; CHD2; WDFY3; chd1; Bchs; Kis

Introduction

Autism Spectrum Disorder (ASD) is a polygenic disorder with a complex underlying genetic etiology (Bourgeron, 2015). Advances in whole genome sequencing and genome-wide association studies have dramatically expanded our understanding of the genetic architecture of ASD. In particular, the identification of rare *de novo* mutations that confer high risk for ASD has generated new molecular insight (De Rubeis et al., 2014; Iossifov et al., 2014; Sanders et al., 2015). Yet, even in cases where a rare *de novo* mutation confers risk for ASD, additional processes are likely to contribute to the ASD phenotype including the engagement of adaptive physiological mechanisms that respond to the presence of an ASD risk associated gene mutation (Gaugler et al., 2014; Gibson, 2009; Hartman et al., 2001; Hou et al., 2019; Kitano, 2007; Plomp et al., 1992; Sackton and Hartl, 2016; Sardi and Gasch, 2018).

Homeostatic plasticity, in particular, has garnered considerable attention as an adaptive physiological process that might be relevant to the phenotypic penetrance of ASD mutations (Antoine et al., 2019; Bourgeron, 2015; Mullins et al., 2016; Nelson and Valakh, 2015; Ramocki and Zoghbi, 2008). Yet, very little is known at a mechanistic level regarding the interface of homeostatic plasticity and ASD genetics. There remains ongoing debate regarding whether homeostatic plasticity is normally induced or whether it is impaired in the context of rare *de novo* mutations that confer risk for ASD (Antoine et al., 2019; Bourgeron, 2015; Ramocki and Zoghbi, 2008). And, there is no mechanistic information regarding how rare *de novo* mutations that confer risk for ASD might be connected to the signaling mechanisms that are essential for the induction and expression of homeostatic plasticity.

It is well established that homeostatic signaling systems function throughout the central and peripheral nervous systems to stabilize neural function following a perturbation that can be of genetic, immunological, pharmacological or environmental origin (Davis, 2006; Marder, 2011; Turrigiano, 2011). Evidence for this has accumulated by measuring how nerve and muscle respond to the persistent disruption of synaptic transmission, ion channel function or neuronal firing. In systems ranging from *Drosophila* to human, cells have been shown to restore baseline function in the continued presence of these perturbations by rebalancing ion channel expression, modifying neurotransmitter receptor trafficking and modulating neurotransmitter release (Davis, 2013; Hengen et al., 2013; Maffei and Fontanini, 2009; Watt and Desai, 2010). There is evidence that homeostatic signaling systems function at the level of individual cells and synapses (Davis, 2013). There is also evidence that homeostatic signaling systems influence the function of neural circuitry (Deeg and Aizenman, 2011; Hengen et al., 2013; Maffei and Fontanini, 2009; Nelson and Valakh, 2015).

We set out to determine whether there exists a molecular interface between mutations in ASD gene orthologs in *Drosophila* and the induction or expression of presynaptic homeostatic plasticity. Presynaptic homeostatic plasticity (PHP) is an evolutionarily conserved form of homeostatic plasticity,

observed in *Drosophila*, mice and humans (Davis, 2013). PHP has been documented at both central and peripheral synapses in response to differences in target innervation (Liu and Tsien, 1995) altered postsynaptic excitability (Davis, 2006; Marder and Goaillard, 2006; Mullins et al., 2016), following chronic inhibition of neural activity (Kim and Ryan, 2010; Zhao et al., 2011) and following disruption of postsynaptic neurotransmitter receptor function (Henry et al., 2012; Jakawich et al., 2010). The mechanisms of PHP have a remarkable ability to modulate and stabilize synaptic transmission, with an effect size that can exceed 200% (Müller and Davis, 2012; Ortega et al., 2018).

Many of the rare *de novo* mutations that confer high risk for ASD are considered to be heterozygous loss of function (LOF) mutations (Bourgeron, 2015; De Rubeis et al., 2014; Iossifov et al., 2014; Sanders et al., 2015). Therefore, we examine the phenotype of heterozygous LOF mutations in five different ASD gene orthologs. We make several fundamental advances. First, we demonstrate that these individual heterozygous LOF mutations have no overt effect on baseline transmission or PHP. However, we demonstrate that PHP is sensitized to failure. Next, we sought to define the molecular mechanisms that connect ASD gene orthologs to the mechanisms of PHP. A genome-scale screen and subsequent systems-genetic analyses yielded unexpected insight. We do not simply identify genes that, when mutated, enhance the phenotype of individual ASD gene mutations. We discovered genes that, when their function is diminished by heterozygous LOF mutations, *commonly modify* multiple ASD gene orthologs, causing a selective failure of homeostatic plasticity. Thus, we define the first class of common phenotypic modifiers of ASD genes in any system. Finally, we do not stop with the identification of a novel class of ASD gene modifiers. We proceed to characterize *how* homeostatic plasticity fails in one such condition. The mechanism we discovered is also unexpected and illuminates the complexity by which double heterozygous gene-gene interactions can generate a cellular or organismal phenotype. We demonstrate maladaptive, enhanced expression of a gene known as *Cellular Repressor of E1A Stimulated Genes (CREG)*, a gene that is conserved from *Drosophila* to human and expressed in the brain (Yang et al., 2011).

Taken together, we define a novel, unexpected genetic architecture that connects heterozygous LOF mutations in ASD-associated gene orthologs with the mechanisms of homeostatic plasticity. In particular, the observation that PHP is commonly sensitized by multiple, different ASD genes, and the fact that we identify and characterize common phenotypic modifiers of five different ASD genes, defines a novel means by which a diversity of ASD-associated risk genes may converge to affect synaptic transmission. We propose that this information may be relevant to new therapeutic approaches that might someday modify ASD phenotypic severity, regardless of the underlying genetic mutation(s) that confer risk for ASD.

Results

We began an investigation of ASD gene orthologs in *Drosophila* by acquiring heterozygous null mutations in five genes; *RIMS1*, *CHD8*, *CHD2*, *WDFY3* and *ASH1L* (Figure 1A; Note: throughout we use the human nomenclature). Heterozygous null mutations were analyzed, as opposed to use of RNAi-mediated gene knockdown, in order to more precisely reflect the proposed genetic perturbations in human. All five of these genes are considered high confidence 'category 1' ASD-associated genes based on SFARI Gene (Simons Simplex Collection, 2020). All five of these genes have clear *Drosophila* orthologs. Further, we demonstrate that all five genes are expressed in *Drosophila* third instar motoneurons based on a Patch-Seq analysis of gene expression (Figure S1). The five ASD gene orthologs were also chosen to reflect a broad range of biological activities that are associated with the numerous ASD-associated genes identified to date. The *RIMS1* gene is a synaptic scaffolding protein that localizes to and organizes sites of neurotransmitter release, termed active zones. The *CHD8* and *CHD2* genes encode chromatin remodeling factors that localize to the cell nucleus. *WDFY3* encodes a phosphatidylinositol 3-phosphate-binding protein and regulator of autophagy and intracellular signaling. *ASH1L* encodes a member of the trithorax group of transcriptional activators and is found in the cell nucleus. A survey of biochemical and genetic interaction networks in *Drosophila* demonstrates no known interactions among these five genes (Flybase). In humans, there appear to be no known direct biochemical interactions among these genes. Yet, heterozygous LOF mutations in each of these genes are associated with risk for ASD in humans.

Heterozygous ASD gene mutations have normal synaptic transmission and PHP

We analyzed baseline neurotransmission and presynaptic homeostatic plasticity (PHP) at the *Drosophila* neuromuscular junction (NMJ) as a model glutamatergic synapse. At the *Drosophila* NMJ, PHP is induced by application of sub-blocking concentrations of the postsynaptic glutamate receptor antagonist philanthotoxin-433 (PhTx; 5-10μM), diminishing the average postsynaptic depolarization caused by the release of single synaptic vesicles (miniature excitatory postsynaptic potential; mEPSP). Decreased mEPSP amplitude initiates a potentiation of presynaptic neurotransmitter release that precisely offsets the magnitude of the PhTx perturbation and, thereby, maintains evoked excitatory postsynaptic potential amplitude (EPSP) at baseline levels prior to the application of PhTx (Figure 1B-E) (Davis, 2013; Frank et al., 2009).

First, we characterized baseline synaptic transmission and the rapid induction of PHP in heterozygous null mutations of all five ASD-associated genes, defined above. We find no significant change in baseline neurotransmission, including average mEPSP amplitude, average EPSP amplitude and quantal content (Figure 1B-E). Following application of PhTx, we find that heterozygous null mutations

in all five ASD gene orthologs do not alter the expression of PHP (Figure 1B-E). Specifically, PhTx significantly diminished the average mEPSP amplitude in each heterozygous mutant and induced a statistically significant increase in quantal content that restored EPSP amplitudes toward wild type values. We conclude that all five heterozygous mutations express normal PHP.

Genetic interaction of *RIMS1* with *CHD8* and with *ASH1L* causes PHP to fail.

Tests of genetic interaction are commonly used to determine if two genes have a function that converges on a specific biological process. While genetic interactions cannot be interpreted to reflect participation in a linear signaling pathway, such an analysis can define signaling relationships among genes that are independent of whether the encoded proteins interact biochemically. Thus, genetic interactions have been a powerful means to explore new signaling systems in model organisms, an approach that is being increasingly utilized in cancer biology (Ashworth et al., 2011; Mair et al., 2019; Chan et al., 2011; O'Neil et al., 2017; Baetz et al., 2004; Bharucha et al., 2011). One approach, formally termed '*second site non-complementation* (SSNC)' or '*non-allelic non-complementation'*, is particularly powerful when a gene of interest is essential for cell or organismal viability, such as *CHD8* and *CHD2*. In brief, if two heterozygous null mutations, each having no observable phenotype when tested alone, create a phenotype when combined in a single organism, then the genes are said to genetically interact according to SSNC. We apply this approach here.

The *Drosophila RIMS1* ortholog was previously demonstrated to be a central component of the presynaptic machinery necessary for PHP (Müller et al., 2012). Genetic interactions with heterozygous null mutations in *Drosophila RIMS1* have been used to link genes to the mechanism of PHP (Harris et al., 2018; Hauswirth et al., 2018; Ortega et al., 2018). First, we confirm that PHP is robustly expressed in the *RIMS1/+* heterozygous null mutant (Figure 1E-G). The average magnitude of homeostatic compensation is indistinguishable from wild type ($p>0.1$). When we plot the relationship between mEPSP amplitude and quantal content for every individual recording, there is a strong negative correlation observed in both wild type ($R^2=0.66$) and *RIMS1/+* ($R^2=0.64$) (Figure 1F and G, respectively).

Next, we analyzed the heterozygous *CHD8/+* mutant, which also shows robust PHP (Figure 1C-E) and a strong negative correlation between mEPSP amplitude and quantal content ($R^2=0.75$; Figure 1H, gray points and black line). However, animals harboring heterozygous mutations in both *RIMS1* and *CHD8* (*CHD8/+; RIMS1/+*) show a complete failure of PHP (Figure 1H). The correlation of mEPSP amplitude and quantal content is abolished (Figure 1H, red points and red line; $R^2=0.01$). The percent homeostasis in the double heterozygote is decreased to less than 10%, not statistically different from baseline (Figure 1H, box; $p=0.6$), and highly statistically different from both *CHD8/+* and *RIMS1/+* alone ($p<0.01$). We conclude that *CHD8* can be linked, directly or indirectly, to the mechanisms of PHP. We

propose that the heterozygous LOF mutation in *CHD8* weakens the robustness of PHP, thereby associating an ASD-associated chromatin remodeling factor with homeostatic mechanisms that ensure robust synaptic transmission.

Next, to test the generality of this effect, we created double heterozygous mutant combinations of *RIMS1*/+ with the remaining ASD orthologs that we examine in this study (*ASH1L*, *CHD2* and *WDFY3)* (Figure S2). The *ASH1L*/+, *RIMS1*/+ double heterozygous animal shows a complete failure of PHP (Figure S2B). The percent PHP expression is decreased from 152% in the *ASH1L*/+ mutant, to 114% in the double heterozygote, which is not different from baseline ($p=0.2$) and represents a highly significant suppression ($p<0.01$) compared to the *ASH1L*/+ mutant alone ($p<0.01$) (Figure S2B). A similar analysis of the *CHD2*/+; *RIMS1*/+ double heterozygous animal shows a significant suppression of PHP ($p=0.01$), although significant PHP remains expressed in the double heterozygous animals (Figure S2C). Finally, the *WDFY3*/+; *RIMS1*/+ double heterozygous animal shows robust PHP (Figure S2D) that is indistinguishable from either the *WDFY3*/+ or the *RIMS1*/+ single heterozygotes. Taken together, these results suggest that there may be an unexpected connection between three unrelated ASD gene orthologs (*CHD8* and *CHD2* and *ASH1L*) and the mechanisms of PHP, given that all three genes interact with *RIMS1*. Based on these data, we pursued a genome-scale forward genetic screen to interrogate and better define the molecular interface of these ASD gene orthologs and the rapid induction of PHP.

Forward genetic screen for altered baseline transmission and PHP

The screen that we performed is diagrammed in Figure 2A. We took advantage of a collection of small chromosomal deficiencies (5-50 genes per deficiency, each with known chromosomal breakpoints; listed in Supplemental Table 1) that tile the 3rd chromosome, uncovering approximately 6000 genes in total. For every double heterozygous combination of *RIMS1*/+ with a heterozygous deficiency, we performed multiple (n=3-15) intracellular recordings, quantifying mEPSP amplitude, EPSP amplitude, quantal content (EPSP/mEPSP), resting membrane potential and input resistance. Recordings were made in the presence of PhTx to induce PHP. If the baseline EPSP is normal and quantal content is increased compared to wild type, then we can conclude that PHP is normally expressed. In these instances, we expect that baseline transmission was also normal in the absence of PhTx. However, if EPSPs are diminished in a given genetic combination (*RIMS1*/+, *Df*/+) and quantal content is not increased compared to wild type, then there are two possible origins: 1) the double mutant impairs baseline transmission or 2) baseline transmission is normal and PHP is selectively impaired. In these instances, the double heterozygous mutant combinations were re-assessed in the absence of PhTx to test for altered baseline transmission.

Double heterozygous combinations that strongly affected muscle resting potential or input

resistance were not observed. We uncovered two instances where a mutant combination (*RIMS1/+, Df/+*) caused a specific deficit in baseline transmission, without altering PHP. We did not isolate any double heterozygous conditions with dramatic defects in mEPSP amplitude. The majority of double mutant combinations specifically affected the expression of PHP. This was unexpected.

Double mutant combinations were determined to disrupt PHP by satisfying one of two criteria. First, the average quantal content (+PhTx) had to be more than one standard deviation below the population mean of all genotypes (Figure 2B, solid horizontal black line). Second, average quantal content had to reside outside a boundary that encompasses 95% of all individual recordings made in the *RIMS1/+* mutant alone (Figure 2B, black dashed lines). Two example 'hits' are shown in red (Figure 2B; dark red point shows data in the absence of PhTx and light red point shows data recorded in the presence of PhTx, and the red lines simply connect the points for a given genotype for the purposes of data display). We also present a complete data set for a single hit from the screen as a standard format bar graph with representative traces (Figure 2D, E). Note that the heterozygous deficiency has normal baseline transmission and PHP ($p>0.1$ One-way ANOVA with post-hoc Tukey multiple comparison), but when combined with a heterozygous mutation in *RIMS1*, PHP completely and selectively fails.

In total, our screen identified, and we subsequently confirmed, 20 small deficiencies that cause PHP to fail when combined with *RIMS1/+*. The identified deficiencies are randomly distributed across the 3rd chromosome (Figure 2C). The screen was empirically validated by the identification, blind to genotype, of deficiencies that uncovered the *RIMS1* locus, as well as the *Pi3K68D* locus (not included in hit list), previously shown to interact as a double heterozygous mutant with *RIMS1/+* (Hauswirth et al., 2018). Furthermore, the *rim binding protein* (RBP) locus was not identified as disrupting PHP, consistent with the previously published observation that a *rbp/+* mutant does not interact with *RIMS1/+* for PHP (Müller et al., 2015). However, *rbp/+* did interact with *RIMS1/+* for baseline neurotransmitter release as expected based on previously published data (not shown) (Müller et al., 2015). No other genes previously implicated in the mechanisms of PHP were present in the deficiencies isolated in our screen. It is important to note that, according to a formal genetic analysis, no strong conclusion can be made regarding the negative result of a double heterozygous genetic interaction.

Finally, we assessed whether there was any relationship between the number of genes that were deleted within a given deficiency and the robustness of PHP. One hypothesis is that the additive effects of multiple, heterozygous gene mutations would increase for larger deficiencies and PHP would be increasingly compromised. That was not the case (Figure 3). There was no correlation between the number of genes uncovered by a given deficiency and EPSP amplitude recorded in the presence of PhTx ($R^2 = 0.003$; Figure 3A). Thus, impaired PHP cannot be accounted for by a simple additive accumulation of genetic mutations within a given deficiency.

Identification of common phenotypic enhancers of multiple unrelated ASD genes

The results of our forward genetic screen, encompassing approximately one third of the *Drosophila* genome, might identify genetic interactions specific to *RIMS1*. However, we reasoned that because *RIMS1* also showed a strong genetic interaction with *CHD8,* as well as *CHD2* and *ASH1L* (Figure 1; Figure S2), a portion of the hits from our screen might also interact with these genes. When initial experiments confirmed that this was the case, we expanded our analysis to encompass all five of the ASD-associated gene orthologs from Figure 1. Thus, we performed a systems-genetic test of all possible double heterozygous genetic interactions, using wild type and the five ASD gene orthologs introduced in Figure 1 combined with wild type and five hits (deficiencies) randomly selected from our forward genetic screen. In total, we tested 36 genetic combinations for baseline transmission and PHP, recording every genotype in the presence and absence of PhTx (Figure 4).

To facilitate visual interpretation, genetic interaction data are presented as a heat map superimposed on a matrix representing all genetic combinations, in the presence or absence of PhTx (Figure 4A). All but one genotype responded to the application of PhTx with decreased mEPSP amplitudes (Figure 4A, mEPSP; compare top left matrix with top right matrix, the transition from blue to red indicates diminished average mEPSP for each genetic combination). Thus, we induced homeostatic pressure in 35 out of 36 genetic combinations (*CHD8/+* with *Df(3)7562/+* being the exception). Next, we demonstrate that all heterozygous deficiencies (x-axis) or heterozygous ASD-associated gene mutations (y-axis), when crossed to the wild type strain (*w1118*) showed normal EPSP amplitudes in the absence and presence of PhTx, demonstrating robust induction of PHP (Figure 4A, EPSP, bottom right matrix). Next, nearly all (23 out of 25) of the double heterozygous combinations show normal EPSP amplitudes in the absence of PhTx, demonstrating normal baseline neurotransmission (Figure 4A, bottom left matrix). However, a majority (16 of 25) of the double heterozygous genetic combinations showed a failure of PHP in the presence of PhTx (Figure 4A, red and light-red boxes, bottom right matrix). In Figure 4B, we also plot the induction of PHP for each double heterozygous combination by calculating the percent change in quantal content following PhTx application (Figure 4B, top matrix). Here, if quantal content does not change (<15% change; gray), then PHP is impaired or blocked. Moderate increases in quantal content (15-30% change; light orange) suggest suppression of PHP, in some instances being statistically significant suppression (see below).

We performed statistical analyses for each double mutant combination, asking whether there was a statistically significant increase in quantal content for a given double mutant in the presence of PhTx compared to that same double mutant combination in the absence of PhTx (Figure 4B, bottom matrix.) Note that we are testing whether PHP is induced in a given double heterozygous mutant combination (an

individual square in the matrix), comparing quantal content in the absence and presence of PhTx. We do not compare PHP expression among different double heterozygous mutant combinations. The colors gray and 'light pink' each reflect a complete block of PHP, an effect that is observed in the majority of double mutant combinations. As a complementary statistical analysis, we tested the differences between individual genotypic conditions (quantal content in each box) versus the wild type quantal content (One-way ANOVA with Dunnett's multiple comparisons) (Figure S3). In this case, if PHP is blocked, then there will be a statistically significant difference compared to wild type. Again, 18 of 25 comparisons are significantly different. The genotypic comparison against wild type verified the analysis based on individual genotypic comparisons (Figure 4B). It should be noted that, in a few instances, minor differences were observed caused by a change in quantal content that was significant (-/+PhTx), but which remained smaller compared to wild type and therefore became significant. Thus, comparisons within genotypes (-/+PhTx) seem to assess the presence or absence of PHP most accurately (Figure 4B).

Our data demonstrate that four out of five deficiencies, isolated in our forward genetic screen as interacting with *RIMS1*, also cause PHP to fail when combined with any one of four different heterozygous ASD-associated gene mutations (Figure 4B, bottom). The pattern of PHP blockade is not uniform. *WDFY3, CHD8* and *CHD2* show a common pattern of interactions with the same three deficiencies. However, *ASH1L* interacts with only two out of the five tested deficiencies. Notably, the five ASD gene orthologs do not share any known common biological activity. Therefore, the identification of common genetic modifiers is completely unexpected. To our knowledge, this is the first demonstration, in any system, of common phenotypic enhancement for multiple, independent and unrelated ASD gene orthologs.

In Figure 4C-F, we elaborate on three of the genetic interactions with data presentations that are more detailed. We show evidence of normal PHP in *CHD8/+* (Figure 4C, replicated from Figure 1). In the adjacent graph (Figure 4C, right), we show evidence of a strong disruption of PHP in the double heterozygous combination of *CHD8/+* with a heterozygous deficiency (*Df(3)24410/+*) isolated in genetic screen. A similar analysis is presented for the *ASH1L/+* heterozygous gene mutation and the interaction with a different heterozygous deficiency (Figure 4D). Finally, a third genetic interaction is presented in a format that is standard for the field of homeostatic plasticity (Figure 4E, F), inclusive of representative traces (Figure 4E) and bar graphs with associated statistical analyses (Figure 4F). Note that values for all recordings are presented (Table S2). Several additional controls were performed to validate and extend the findings reported for our genetic interaction data set. First, we note that all double heterozygous mutant combinations are adult viable. Thus, it was possible to inspect adult animals for phenotypes that might indicate altered signaling. Inspection of the compound eye and wings (bristles, wing veins and size) demonstrate wild type tissue morphogenesis (data not shown).

312

313 ***PDPK1* and *PPP2R5D* are common phenotypic enhancers of multiple ASD gene orthologs**

314 We isolated the causal single gene mutations within two of the deficiencies isolated from our
315 screen. To do so, we tested smaller sub-deficiencies that mapped within the originally isolated
316 deficiencies. Sub-deficiency mapping either identified the causal gene, or a limited number of candidates.
317 We subsequently tested individual gene candidates with established single gene mutations or RNAi. The
318 process of mapping to single genes, therefore, included several rounds of independent phenotype
319 verification. The first two instances in which we have isolated single causal genes are presented. Each
320 candidate gene was tested individually against all five ASD gene orthologs, using previously published
321 mutations (Figure 5). For both genes, we confirmed the same set of genetic interactions that occurred
322 when analyzing the deficiency that included the identified gene (Figure 5).

323 The first gene that we identified encodes a serine threonine kinase encoded by the *PDPK1* gene
324 (*PDK1* in *Drosophila*). *PDPK1* is a master controller of cellular metabolism, as well as cellular and
325 synaptic growth at the *Drosophila* NMJ (Cheng et al., 2011). The second gene encodes a regulatory
326 subunit of the PP2A phosphatase encoded by the *PPP2R5D* gene (*wrd* in *Drosophila*) (Viquez et al.,
327 2006). *PPP2R5D* is also a master controller of cellular metabolism (Bernal et al., 2014), as well as
328 cellular and synaptic growth at the *Drosophila* NMJ (Viquez et al., 2006). Both proteins are present at the
329 *Drosophila* NMJ (Cheng et al., 2011; Viquez et al., 2009, 2006) Single-cell Patch-Seq experiments
330 confirmed the expression of these genes in *Drosophila* motoneurons at third-instar (Figure S1).
331 Intriguingly, the *PPP2R5D* gene has recently been associated with intellectual disability and autism in
332 human (Loveday et al., 2015; Shang et al., 2016).

333 Next, we demonstrate that both genes, *PDPK1* and *PPP2R5D,* are common modifiers of multiple
334 heterozygous ASD-associated gene mutations (Figure 5). To underscore the specificity of the double
335 heterozygous genetic interactions (Figure 5B, E), we restored the expression of the *CHD2* gene to wild
336 type levels in the *CHD2/+; PPP2R5D/+* double heterozygous combination. This was achieved using a
337 previously published translocation of the *CHD2* gene locus that allowed us to put back one copy of the
338 *CHD2* gene ($CHD2^{WT}$/+) in the background of the *CHD2/+*; *PPP2R5D*/+ double mutant. We demonstrate
339 that PHP is fully restored (Figure 5C). An identical series of experiments was performed with a
340 previously characterized *PDPK1* mutation (Figure 5E, F). Thus, *PDPK1* and *PPP2R5D* represent the first
341 known common phenotypic modifiers of ASD gene orthologs, causing PHP to fail. The data also
342 underscore that deficiencies isolated in our forward genetic screen can be resolved to the activity of single
343 genes. As such, the screen may have identified a novel class of common phenotypic modifier.

344 Another series of control experiments were performed to test the specificity of these genetic
345 interactions. First, given that both *PDPK1* and *PPP2R5D* affect synaptic growth as homozygous null

mutations, we asked whether neuronal morphology was substantially altered in the double heterozygous mutant combinations of *PDPK1* or *PPP2R5D* with each ASD-associated gene ortholog. This was not the case. Altered NMJ growth was not commonly observed in the majority of genetic interactions tested (Figure S4). We do find evidence that the heterozygous *CHD8*/+ mutation predisposes the NMJ to modest overgrowth, consistent with *CHD8* influencing brain development in other systems (Gompers et al., 2017). But, there was no synergistic or common effect that correlated with widespread block of PHP. Thus, we conclude that altered synaptic growth is not the cause of common PHP failure.

Deletion of *PPP2R5D* impairs the robustness of PHP

Given that *PPP2R5D* and *PDPK1* both genetically interact with multiple ASD-associated gene mutations, and given that several of the ASD-associated genes sensitize PHP toward failure, we considered whether *PPP2R5D* and *PDPK1* are also directly involved with the induction of PHP. Unlike many of the ASD genes, both *PPP2R5D* and *PDPK1* are viable as homozygous deletion mutations, allowing a direct test of their involvement in PHP. To our surprise, neither *PPP2R5D* nor *PDPK1* can be classified as strictly essential for the mechanisms of PHP based on analysis of homozygous LOF mutants (Figure S5). PHP is fully expressed in the homozygous *PDPK1* mutant (Figure S5), demonstrating that this gene is not required. There is a statistically significant suppression of PHP in the homozygous LOF mutation in *PPP2R5D* suggesting a role for this gene in the rapid induction of PHP, but without being strictly necessary (Figure S5).

We note that both *PDPK1* and *PPP2R5D* control signaling that directly intersects with the AKT/mTOR pathway, a signaling system that is associated with ASD in human (Alessi et al., 1997; Manning and Toker, 2017; Yeung et al., 2017). The mTOR signaling proteins *S6K* and *Tor* have both been implicated in the long-term maintenance of PHP. However, both are dispensable for the rapid, PhTx-dependent induction of PHP (Cheng et al., 2011; Penney et al., 2012). Never-the-less, the possible connection to Tor signaling prompted us to revisit our screen data and ask whether mutations affecting the broader AKT/mTOR signaling system might also be common ASD-gene modifiers. The genes *Akt, S6K, TSC1, TSC2,* and *PTP61F* are all encoded on the *Drosophila* third chromosome. All of these genes were present within the deficiencies that were tested in our screen. But, none were identified as a hit in our unbiased forward genetic screen. Although the lack of a genetic interaction cannot be used to conclude the absence of a role for these genes in the PHP effects that we observe, it seems likely that *PPP2R5D* and *PDPK1* have other targets relevant to the intersection of ASD-gene mutations and the rapid induction of PHP. Consistent with this possibility, *PDPK1* and *PPP2R5D* are predicted to have opposing actions on AKT, yet both genes participate in the blockade of PHP when combined with a mutation in one of the five ASD-associated gene mutations (see discussion). Furthermore, as demonstrated below, one

mechanism by which PHP is blocked is novel and unexpected.

Dissecting the mechanism of impaired PHP in a single double heterozygous mutant combination

It is rare for a genetic study to define, precisely, how a double heterozygous interaction creates a synthetic phenotype if the two genes do not encode proteins that biochemically interact. Simply put, there are a vast number of possible mechanisms by which SSNC could occur (Yook et al., 2001). None-the-less, we attempted to do so for at least one double heterozygous combination. Although this represents only a single mechanism of SSNC, it could provide proof of principle for how PHP is affected in other ASD gene interactions. We chose the genetic interaction of *PPP2R5D/+* with *CHD8/+*. This combination was chosen because *CHD8* is among the most common ASD *de novo* gene mutations. Furthermore, the genetic interaction is highly penetrant.

We began by pursuing additional phenotypic analyses, looking for clues in a wider variety of cellular and electrophysiological measures. It is possible that the genetic interaction of *PPP2R5D/+* with *CHD8/+* could indirectly affect PHP expression by altering motoneuron firing properties. Therefore, we analyzed intrinsic excitability and neuronal firing by patch clamp electrophysiology of larval motoneurons. There is no change in motoneuron firing frequency in response to a series of step current pulse injection. Likewise, there are no changes in action potential amplitude, cell input resistance or rheobase comparing wild type with each single heterozygous mutation and the double heterozygote (Figure S6). Thus, aberrant excitability is not linked to impaired PHP.

Ultrastructural correlate of impaired PHP: altered presynaptic membrane trafficking

Next, we turned to electron microscopy to determine whether the genetic interaction of *PPP2R5D/+* with *CHD8/+* affects the presynaptic release site. Ultrastructural changes have previously been linked to impaired PHP (Harris et al., 2018). Thin section transmission electron microscopy was used to examine the synapse, defined as a characteristic increase in pre- and postsynaptic membrane electron density, opposing clustered presynaptic vesicles and a characteristic presynaptic density, termed a T-bar. We find that the ultrastructure of *CHD8/+* alone was wild type (Figure 6B, D, E). The ultrastructure of *PPP2R5D/+* alone was wild type (Figure 6A, D, E). However, the double heterozygous mutant showed evidence of large membrane structures surrounding the presynaptic release site and apparent stalled endocytic events, appearing adjacent to sites of neurotransmitter release where compensatory synaptic vesicle endocytosis occurs (Figure 6C, insets). Quantification of vesicle size reveals a large increase in average intracellular vesicle diameter for all vesicles within 150nm of the base of the presynaptic release site, defined by the T-bar structure (Figure 6D, E), again selective to the double heterozygous mutant. These data provide a striking visual confirmation of the genetic interaction between

414 *PPP2R5D/+* and *CHD8/+*. And, this is further evidence linking the action of a chromatin-remodeling
415 factor (CHD8) to the stability of synaptic transmission.
416 Given the appearance of enlarged vesicles at or near the presynaptic release site, we repeated our
417 ultrastructural analysis of the double heterozygous mutant, fixing the synapse immediately (~1-5 sec)
418 after strong stimulation of presynaptic release (50Hz stimulation, 10seconds). In wild type, there was no
419 change in the number or appearance of presynaptic vesicles when fixed immediately following the
420 stimulus. However, in the double heterozygous mutant condition (*CHD8/+; PPP2R5D/+*) we found that
421 intracellular vesicles were further increased in size and took on a crenulated appearance (Figure 6F-I).
422 These data are consistent with the enlarged vesicles being endosomal intermediates, arguing that the
423 process of vesicle recycling is altered in the double heterozygous mutant. In further support of this idea,
424 we demonstrate enhanced synaptic depression in response to high frequency (50Hz) stimulation (Figure
425 S7). Regardless of the underlying molecular mechanism leading to this EM phenotype and associated
426 physiological deficits (a topic for future study), these data present a striking, visual confirmation of a
427 strong synthetic genetic interaction between *PPP2R5D/+* and the *CHD8/+* heterozygous mutations.
428 Furthermore, these data link the activity of a chromatin remodeling factor, present in the nucleus (CHD8),
429 to a profound synaptic defect. Experiments detailed below, including genetic rescue, confirm the
430 specificity of this EM phenotype.
431
432 **Differential gene expression analyses**
433 One possible reason that genes isolated from our screen are common modifiers of diverse ASD
434 genes is that each modifier is a direct transcriptional target of the ASD mutants. It is possible to assess
435 this by RNAseq. To our knowledge, side-by-side differential gene expression analysis has yet to be
436 performed for multiple heterozygous ASD-associated gene mutant backgrounds. We performed whole
437 genome RNAseq analysis for wild types and the four heterozygous ASD mutants (four biological
438 replicates) (Figure 7A). We asked whether any of the genes contained within the 20 deficiencies
439 identified in the screen (37 genes) are commonly altered in all four of ASD-associated mutants (Figure
440 7A, orange data points). None were commonly differentially regulated (p-value=0.096 for *ASH1L/+*; p-
441 value=0.636 for *WDFY3/+*; p-value=0.392 for *CHD2/+*; p-value=0.112 for *CHD8/+*; Wilcoxon sign rank
442 test two-sided). We conclude that common down-regulation of identified genetic modifiers cannot
443 account for the common impairment of PHP that we observe electrophysiologically.
444 Next, we asked whether the ASD-associated gene mutations might cause common changes in
445 gene expression, with potential relevance to a common disruption of PHP. We define all differentially
446 expressed genes common to at least two ASD mutations (Figure 7B, C). While there are individual genes
447 that are commonly differentially regulated, a GO database analysis of differentially expressed genes did

not reveal any consistent change in a gene category across all four genotypes. The patterns of gene dysregulation do not predict any pattern of genetic interactions documented in our systems-genetic analysis. Finally, while there are genes that are commonly dysregulated in multiple ASD gene orthologs, there are only two genes that are commonly down-regulated in all four ASD mutants (*FBgn0027578* [*Nepl21*] and *FBgn0037166* [*CG11426*]) (Figure 7C). *FBgn0027578* encodes a metalloprotease of the Neprilysin family, with homology to endothelin converting enzyme 1 in human, of unknown function in the nervous system. *FBgn0037166* encodes phosphatidic acid phosphatase type 2, which is expressed in the *Drosophila* nervous system, but of unknown function. There is no obvious means to connect the down regulation of these two genes to impaired homeostatic signaling, although future experiments will explore these genes in greater depth. Furthermore, there is no clear connection, biochemically or genetically, to the role of *PDPK1* or *PPP2R5D* in the nervous system. Thus, a transcriptional analysis of heterozygous ASD gene mutations alone did not allow us to make clear progress toward understanding the mechanisms of impaired PHP.

Candidate mechanisms for impaired PHP based on differential gene expression analysis

Next, we continued with our focus on characterizing the homeostasis defect in the *CHD8/+; PPPR25D/+* double heterozygous mutant combination. We repeated the RNAseq differential gene expression analysis comparing the double heterozygous condition to three control conditions, inclusive of wild type and each single heterozygous mutant alone. In this manner, we sought to identify synergistic effects on gene expression that could not be accounted for in either single heterozygous mutant alone (Figure 7D, E). As expected, many of the differentially expressed genes documented in the double heterozygous mutant, when compared to wild type, could be accounted for by subsequent comparisons to each single heterozygous mutant. However, a small number of genes (14 genes; 5 upregulated and 9 downregulated) appear to be synergistically differentially expressed in the double heterozygous mutant compared to all three control conditions (Figure 7D, E). We successfully replicated altered expression of four genes in the double heterozygous mutant combination by quantitative RT-PCR (Figure 8A, B). Of these genes, *CREG* stood out as being robustly and dramatically up-regulated. Upon closer inspection, *CREG* showed a slight, but significant, up-regulation in the *CHD8/+* mutant (Figure 7A), and this was enhanced by the presence of the heterozygous *PPP2R5D/+* mutation (Figure 7E, left). Next, we confirmed the up-regulation of *CREG* in the third instar larval central nervous system by QPCR (Figure S8B). Finally, we took advantage of a previously published gene expression data set (Parish et al., 2015) and document *CREG* expression in motoneurons throughout embryonic and larval development. *CREG* is strongly expressed in embryonic motoneurons (20-24h after egg laying – AEL), after which expression levels plummet (Figure S8A).

482

483 ***CREG* is a homeostatic repressor.**

484 *CREG* (Cellular Repressor of E1A-stimulated Genes) encodes an endosomal/lysosomal localized
485 glycoprotein that is linked to stress responses in other systems as well as to the homeostatic maintenance
486 of the vascular epithelium (Ghobrial et al., 2018; Kowalewski-Nimmerfall et al., 2014). Mammalian
487 orthologs are expressed in the brain (Yang et al., 2011). However, *CREG* function has never been
488 addressed in the nervous system of any organism. Given that we observe a strong synaptic internal
489 membrane phenotype in the *CHD8+*; *PPP2R5D/+* double heterozygous mutant, and given that CREG
490 localizes to the endo-lysosomal system, we chose to study *CREG* in greater detail, asking if it is causally
491 involved in PHP.

492 Two independent transposon insertion mutations were identified, residing in the *Drosophila*
493 *CREG* gene locus (Figure 8C). The $CREG^{M1}$ transposon completely abolishes *CREG* expression and a
494 heterozygous $CREG^{M1}$/+ mutant reduces *CREG* expression by 50% (data not shown). Next, we generated
495 a triple heterozygous mutant combination (*CHD8+; PPP2R5D/+,* $CREG^{M1}$/+) and find that the
496 $CREG^{M1}$/+ allele attenuates the up-regulation of *CREG* gene transcript in the triple heterozygous mutant
497 background, a suppression effect of approximately 50%, as predicted (Figure 8D). Then, we repeated this
498 analysis with the $CREG^{M2}$ allele and discovered that this transposon insertion caused a complete block of
499 *CREG* up-regulation in the triple heterozygous mutant combination, suggesting that this transposon
500 insertion, residing in 3' UTR, may disrupt a transcription regulatory motif (Figure 8D).

501 Next, we asked whether the triple heterozygous mutant combinations, in which *CREG* up-
502 regulation is either attenuated or abolished, would rescue the expression of homeostatic plasticity and
503 synaptic ultrastructure. In both triple mutant combinations (*CHD8+; PPP2R5D/+*, $CREG^{M1}$/+) and
504 (*CHD8+; PPP2R5D/+*, $CREG^{M2}$/+), the expression of PHP is fully rescued (Figure 8E, F). These data
505 are consistent with the conclusion that the abnormally enhanced levels of *CREG* transcription are
506 responsible for the block of homeostatic plasticity seen in the double heterozygous mutant combination. If
507 true, then we might also see rescue of the ultrastructural phenotype in the *CHD8+; PPP2R5D/+*,
508 $CREG^{M1}$/+ triple mutant. Indeed, this is the case (Figure 8G). We observe full rescue of synaptic
509 ultrastructure. Thus, preventing the dramatic up-regulation of *CREG*, without abolishing *CREG*
510 expression, is sufficient to restore membrane trafficking and PHP to the presynaptic nerve terminal of the
511 *CHD8+; PPP2R5D/+* double mutant combination.

512 It is possible that CREG is a novel suppressor of PHP. However, it is also possible that CREG
513 mediates this effect only in the context of the other two heterozygous mutations. To address this
514 possibility, we generated a *UAS-CREG* transgenic line, allowing cell-type specific overexpression of the
515 *CREG* gene. Over-expression of *CREG* in a wild type background using either a ubiquitously expressed

source of GAL4 (*tubulin-GAL4*), or a GAL4-line that is selective to motoneurons (*OK371-GAL4*), causes a complete block of PHP (Figure 8J-K). As a control for adverse developmental effects of *CREG* overexpression, we analyzed NMJ anatomy and find no substantive effects on NMJ growth or morphology that could account for the absence of PHP (Figure S9). Our data are consistent with the conclusion that *CREG* is a novel homeostatic repressor, one of very few identified to date (Spring et al., 2016). This finding underscores the complexity of interpreting the double heterozygous mutant combinations that cause blockade of PHP.

Assessing the generality of CREG as a mechanism for impaired PHP.

In mammals, there are two *CREG* genes and *CREG2* is expressed in the brain (Yang et al., 2011). A recent study provides evidence that *CREG2* expression is enhanced in layer 4 excitatory neurons, isolated from human postmortem ASD patient brain tissue (Velmeshev et al., 2019), suggesting possible relevant. This fact prompted us to ask whether over-expression *CREG* is the primary mechanism responsible for the disruption of PHP, or whether it is just one of many. Our existing gene expression analysis demonstrates that *CREG* is not up-regulated in the other heterozygous mutations (*ASH1L* or *CHD2* or *WDFY3*; Figure 7). This was extended to the *PDPK1/+* mutant and, again, CREG levels are not increased. Finally, we analyzed two additional double heterozygous mutant combinations (*PDPK1/+* with *CHD2/+* as well as *PPP2R5D/+* with *CHD2/+*). CREG was not up-regulated compared to single heterozygous controls. Finally, we repeated the ultrastructural analysis for a second genetic combination (*PPP2R5D/+* with *CHD2/+*). No phenotype of enlarged vesicles or endomembranes observed (Figure S10). From these data, we conclude that the aberrant over-expression of *CREG* is not a universal cause of impaired PHP in the double heterozygous interactions. In the future, a systematic test of all genetic combinations identified in our screen may define whether CREG over-expression is unique to a single genetic interaction or whether it is reflected in a subset of gene interactions.

Discussion

In this study, we make several fundamental advances. First, we provide evidence that mutations in multiple different ASD-associated genes sensitize homeostatic plasticity to fail (Figure 9A, B). Second, using genome-scale forward genetics and subsequent systems-genetic analyses, we identify the first phenotypic modifiers that *commonly enhance* five different ASD-associated gene mutations, causing a specific failure of PHP (Figure 9A). Third, we identify *PDPK1* and *PPP2R5D* as common phenotypic modifiers of multiple ASD-associated genes and, thereby, define a mechanistic link between synaptic transmission, PHP and chromatin remodeling complexes in the neuronal nucleus (Figure 9A). Finally, we define how PHP fails at the intersection of an ASD-associated gene mutation and phenotypic modifier.

The mechanism is unexpected, involving the maladaptive up-regulation of a novel repressor of homeostatic plasticity (CREG) (Figure 9C). We demonstrate that up-regulation of *CREG* cannot explain other gene-gene interactions, undercoring the potential complexity of gene-gene interactions and the common failure of PHP. Regardless of potential mechanistic complexity, our data argue that impaired PHP may be a common pathophysiological effect downstream of LOF mutations in five different ASD-associated genes. If our data can be extended to additional ASD genes, and to other experimental systems including human neurons, then it may be possible to use this information to advance therapeutic approaches that modify ASD phenotypic severity regardless of the underlying genetic mutation(s) that confer risk for ASD.

The loss or impairment of PHP could contribute to the phenotypic penetrance of an ASD gene mutation in multiple ways. Impaired PHP is expected to render the nervous system less robust to perturbation including the effects of environment stress, immunological stress, or genetic mutation (Davis, 2013, 2006). If an ASD-associated gene mutation leads to neural developmental defects, then loss of PHP would be expected to exacerbate the functional consequences. According to the same logic, loss of PHP might enhance the adverse effects of environmental or immunological stress, both of which are thought to contribute to ASD pathophysiology (Beversdorf et al., 2018; Modabbernia et al., 2017). Finally, loss of PHP could be relevant to the appearance or severity of ASD comorbidities, including epilepsy.

It should be emphasized that failed homeostatic plasticity cannot be determined by simply assessing the phenotype of a heterozygous ASD-associated gene mutation. The observation of a phenotype, such as altered E/I balance or impaired neurotransmission, could reflect failure of homeostatic plasticity, or it could reflect the outcome of successful homeostatic mechanisms that constrained a phenotype that might otherwise have been more severe (Davis, 2013; Kulik et al., 2019). Ultimately, the loss or impairment of homeostatic plasticity can only be determined by a direct test of homeostatic robustness; specifically referring the ability of a neuron, synapse or neural circuit to respond to a perturbation and sustain normal function in the continued presence of the perturbation (Davis, 2013, 2006). Thus, our data set the stage for similar analyses in other model organisms, potentially extending the connection between ASD-associated gene mutations and the robustness of PHP or other forms of homeostatic plasticity.

The specificity of gene-gene interactions that cause PHP to fail

The genetic interactions that we document in our study appear to be highly specific. First, our genetic screen was based on the use of deficiency chromosomes that uncover 5-50 genes each, rendering those genes heterozygous. Thus, each deficiency can be considered to test pairwise gene-gene interactions among all the genes contained in the deficiency. According to this logic, we tested in excess of 50,000

584 double heterozygous gene combinations and discovered only 20 interactions that cause PHP to fail.
585 Although it is unlikely that genes are completely randomly distributed throughout the genome, this
586 calculation still has merit and emphasizes the rarity of gene-gene interactions that cause PHP to fail. In
587 addition, we found no correlation between the number of genes deleted in a heterozygous deficiency and
588 the impairment of PHP. Thus, the likelihood of a genetic interaction does not increase with the number of
589 genes that are rendered heterozygous. Finally, it should be emphasized that PHP is a robust physiological
590 process that is not unusually susceptible to the effects of genetic mutations. Previously, forward genetic
591 have observed low rates of gene discovery. Two such screens tested transgenic RNAi against nearly every
592 kinase and phosphatase encoded in the *Drosophila* genome, a gene set that includes prominent signaling
593 proteins, the majority of which had no effect on PHP induction or expression (Brusich et al., 2015;
594 Hauswirth et al., 2018). With this information as a background, the identification of genes that commonly
595 enhance multiple ASD genes, causing PHP to fail, seems extraordinarily.
596
597 **The rapid induction versus long-term expression of PHP**
598 There are two well-established methods to induce expression of PHP. Application of PhTx
599 induces PHP within minutes, a process that can be maintained for hours (Frank et al., 2006). In addition,
600 a mutation in the non-essential *GluRIIA* subunit of postsynaptic glutamate receptors drives persistent
601 expression of PHP. Since the *GluRIIA* mutation is present throughout the life of the organism, it is
602 inferred that this reflects the long-term maintenance of PHP. Although this distinction reflects only the
603 duration of the perturbation (acute versus genetic), recent work does argue that the acute induction of
604 PHP may transition to another long-term expression mechanism (Harris et al., 2018, 2015). Indeed,
605 screens based on the acute versus long-term PHP have identified different candidate genes, even when
606 screening a common transgenic RNAi collection (Brusich et al., 2015; Hauswirth et al., 2018).
607 It remains unknown whether one form of PHP is more relevant regarding the intersection of
608 homeostatic plasticity with diseases or disorders of the nervous system. In the present study, the acute
609 induction of PHP can be considered a type of 'stress test'. If the rapid induction of PHP fails, we can infer
610 that the neurons are less robust to perturbation. In the future, it will be interesting to systematically
611 determine whether the gene-gene interactions identified here also uniformly perturb PHP induced by the
612 *GluRIIA* mutation. However, such an analysis is beyond the scope of the present study.
613
614 **Common phenotypic enhancers of multiple ASD gene orthologs**
615 How can the existence of common phenotypic modifiers be explained? We began our study with
616 the demonstration that heterozygous LOF mutations in four unrelated genes ASD-associated gene
617 including *RIMS1* (presynaptic scaffolding protein), *CHD8* (chromatin helicase), *CHD2* (chromatin

helicase) and *ASH1L* (transcriptional activator and histone methyltransferase), all sensitize the expression of PHP to fail (Figure 1, Figure S2, Figure 9B). One possibility, therefore, is that PHP is commonly sensitized to fail by heterozygous LOF mutations in each of the five ASD gene orthologs that we chose to study. If so, then a phenotypic modifier that interacts with one of these genes might also be expected to commonly interact with the other ASD genes. In other words, commonality arises because of the unexpected finding that each ASD gene ortholog has an activity that, when diminished, impairs the robustness of PHP. Our data generally support this model, given that three of four ASD genes interact with *RIMS1* to block PHP. According to this model, we provide the first evidence that sensitization of PHP is a common pathophysiological effect downstream of multiple ASD genes with, as yet, unrelated biological activities.

The finding that ASD gene mutations sensitize PHP to fail does not require that each ASD gene participate in the actual mechanisms of PHP. *RIMS1* is a core component that is required for PHP (Müller et al., 2012). However, a gene such as *CHD8* might compromise PHP indirectly by causing some form of cellular stress that interacts with the mechanisms of PHP (Figure 8 J, K). Indeed, it was previously demonstrated that simultaneous induction of two different forms of homeostatic plasticity creates interference and homeostatic failure (Bergquist et al., 2010). The same argument can apply to the novel class of common phenotypic modifiers. Some modifiers may represent core components of PHP, including *PPP2R5D*, which seems to suppress PHP when knocked out (Figure S5). However, the *PDPK1* knockout has no effect on PHP and, therefore, may interact with the mechanisms of PHP indirectly. Thus, we cannot rule out the possibility that compounded cellular stressors occasionally intersect and cause PHP to fail.

Novel mechanisms impair PHP; CREG-dependent suppression of PHP.

We explored, in detail, how PHP fails at the intersection of *CHD8/+* and *PPP2R5D/+*. First, we discovered a profound effect on synaptic ultrastructure that was not observed in either single heterozygous mutation. This provided dramatic visual proof of a strong, genetic interaction between these two heterozygous gene mutations. Next, we demonstrate that this strong, genetic interaction is not a consequence of extensive transcriptional dysregulation. Indeed, when the effects of each heterozygous gene mutation are taken into account, only 14 genes show evidence of altered transcription. A single gene, *CREG*, was subsequently demonstrated to be the cause of impaired PHP and disrupted presynaptic membrane trafficking. Although *CREG2* is not upregulated in the heterozygous *CHD8/+* mouse, a recent study provides evidence that *CREG2* expression is enhanced in layer 4 excitatory neurons, isolated from human postmortem ASD patient brain tissue (Gompers et al., 2017; Velmeshev et al., 2019).

It remains to be determined how loss of *PPP2R5D* causes further dysregulation of *CREG* in the

background of *CHD8/+*. One possibility is that *CREG* is a stress-response gene, and up-regulation occurs at the intersection of two cellular stresses. Other alternatives remain plausible, including a direct connection between *CHD8* and *CREG* that is modulated by PPP2R5D-mediated signaling. The biochemical and transcriptional relationships will be defined in subsequent work and are beyond the scope of our current study. The generality of this genetic interaction will also be explored. We note, for example, that *CREG* shows a mild increase only in the *CHD8/+* mutant, not in the other three ASD-associated genes (Figure 7A). This does not rule out *CREG* participating in genetic interactions involving other ASD-associated genes, but it might suggest additional mechanisms will be engaged.

CREG encodes a glycoprotein that localizes within the endo-lysosomal system and may also be secreted. In mammals, there are two *CREG* genes and *CREG2* is expressed in the brain (Yang et al., 2011). There is generally more information regarding the function of *CREG1,* which is an effector of tissue homeostasis in the vascular epithelium (Ghobrial et al., 2018). In this capacity, CREG seems to function as a stress response factor, influencing the activity of several potent signaling systems (Ghobrial et al., 2018). Our current phenotypic analyses suggest that increased levels of *CREG* may directly impact the integrity of synaptic vesicle membrane recycling and, either directly or indirectly, interface with the homeostatic potentiation of vesicle release. Thus, while a full dissection of *CREG* activity remains for future studies, our data argue that *CREG* has an activity that could be directly coupled to vesicle release and recycling, an ideal situation to normally limit the homeostatic potentiation of vesicle fusion.

Relevance and Conclusions

It is well established that genetic context can profoundly influence the phenotypic severity of disease-causing gene mutations. For example, in mice, it has been shown that genetic context (strain background) influences phenotypic penetrance in an Alzheimer's disease model (Neuner et al., 2019). In humans, systematic screening of the phenotypically normal population has identified individuals that are resistant to the effects of well-established, debilitating disease causing mutations, an effect termed 'resilience' that is attributed to the effects of genetic context (Chen et al., 2016; Friend and Schadt, 2014). It seems plausible that the common phenotypic enhancers, identified in our genetic screen, could represent a mechanism by which genetic context influences the phenotypic penetrance of ASD-associated gene mutations. We recognize that *PDPK1* and *PPP2R5D* have fewer than expected LOF and missense mutations in humans (http://exac.broadinstitute.org). It remains to be determined if this will be the case with additional modifier genes. Furthermore, we note that PHP is completely blocked at the intersection of ASD gene mutations and the common modifiers we identify. Therefore, subtle changes in the expression or function of common phenotypic modifiers, perhaps caused by mutations in enhancer/promoter regions, could impact expression or robustness of PHP with cascading negative

phenotypic consequences. If our findings can be extended to other systems, including humans, it is conceivable that our emerging mechanistic understanding could be used to restore the beneficial effects of homeostatic plasticity and alleviate aspects of ASD phenotype, irrespective of individual genetic makeup.

References

Alessi DR, James SR, Downes CP, Holmes AB, Gaffney PRJ, Reese CB, Cohen P. 1997. Characterization of a 3-phosphoinositide-dependent protein kinase which phosphorylates and activates protein kinase Bα. *Curr Biol* **7**:261–269. doi:10.1016/S0960-9822(06)00122-9

Antoine MW, Langberg T, Schnepel P, Feldman DE. 2019. Increased Excitation-Inhibition Ratio Stabilizes Synapse and Circuit Excitability in Four Autism Mouse Models. *Neuron* **101**:648-661.e4. doi:10.1016/J.NEURON.2018.12.026

Ashworth A, Lord CJ, Reis-Filho JS. 2011. Genetic interactions in cancer progression and treatment. *Cell* **145**:30–8. doi:10.1016/j.cell.2011.03.020

Bergquist S, Dickman DK, Davis GW. 2010. A hierarchy of cell intrinsic and target-derived homeostatic signaling. *Neuron* **66**:220–34. doi:10.1016/j.neuron.2010.03.023

Bernal M, Zhurinsky J, Iglesias-Romero AB, Sanchez-Romero MA, Flor-Parra I, Tomas-Gallardo L, Perez-Pulido AJ, Jimenez J, Daga RR. 2014. Proteome-wide search for PP2A substrates in fission yeast. *Proteomics* **14**:1367–1380. doi:10.1002/pmic.201300136

Beversdorf DQ, Stevens HE, Jones KL. 2018. Prenatal Stress, Maternal Immune Dysregulation, and Their Association With Autism Spectrum Disorders. *Curr Psychiatry Rep* **20**:76. doi:10.1007/s11920-018-0945-4

Bourgeron T. 2015. From the genetic architecture to synaptic plasticity in autism spectrum disorder. *Nat Publ Gr* **16**. doi:10.1038/nrn3992

Brusich DJ, Spring AM, Frank CA. 2015. A single-cross, RNA interference-based genetic tool for examining the long-term maintenance of homeostatic plasticity. *Front Cell Neurosci* **9**:107. doi:10.3389/fncel.2015.00107

Chan DA, Giaccia AJ. 2011. Harnessing synthetic lethal interactions in anticancer drug discovery. *Nat Rev Drug Discov* **10**:351–64. doi:10.1038/nrd3374

Chen R, Shi L, Hakenberg J, Naughton B, Sklar P, Zhang J, Zhou H, Tian L, Prakash O, Lemire M, Sleiman P, Cheng W, Chen W, Shah H, Shen Y, Fromer M, Omberg L, Deardorff MA, Zackai E, Bobe JR, Levin E, Hudson TJ, Groop L, Wang J, Hakonarson H, Wojcicki A, Diaz GA, Edelmann L, Schadt EE, Friend SH. 2016. Analysis of 589,306 genomes identifies individuals resilient to severe Mendelian childhood diseases. *Nat Biotechnol* **34**:531–538. doi:10.1038/nbt.3514

720 Cheng L, Locke C, Davis GW. 2011. S6 kinase localizes to the presynaptic active zone and functions
721 with PDK1 to control synapse development. *J Cell Biol* **194**:921–35. doi:10.1083/jcb.201101042
722 Davis GW. 2013. Homeostatic signaling and the stabilization of neural function. *Neuron* **80**:718–28.
723 doi:10.1016/j.neuron.2013.09.044
724 Davis GW. 2006. Homeostatic control of neural activity: from phenomenology to molecular design. *Annu*
725 *Rev Neurosci* **29**:307–323. doi:10.1146/annurev.neuro.28.061604.135751
726 De Rubeis S, He X, Goldberg AP, Poultney CS, Samocha K, Ercument Cicek A, Kou Y, Liu L, Fromer
727 M, Walker S, Singh T, Klei L, Kosmicki J, Fu S-C, Aleksic B, Biscaldi M, Bolton PF, Brownfeld
728 JM, Cai J, Campbell NG, Carracedo A, Chahrour MH, Chiocchetti AG, Coon H, Crawford EL,
729 Crooks L, Curran SR, Dawson G, Duketis E, Fernandez BA, Gallagher L, Geller E, Guter SJ, Sean
730 Hill R, Ionita-Laza I, Jimenez Gonzalez P, Kilpinen H, Klauck SM, Kolevzon A, Lee I, Lei J,
731 Lehtimäki T, Lin C-F, Ma'ayan A, Marshall CR, McInnes AL, Neale B, Owen MJ, Ozaki N,
732 Parellada M, Parr JR, Purcell S, Puura K, Rajagopalan D, Rehnström K, Reichenberg A, Sabo A,
733 Sachse M, Sanders SJ, Schafer C, Schulte-Rüther M, Skuse D, Stevens C, Szatmari P, Tammimies
734 K, Valladares O, Voran A, Wang L-S, Weiss LA, Jeremy Willsey A, Yu TW, Yuen RKC, Cook EH,
735 Freitag CM, Gill M, Hultman CM, Lehner T, Palotie A, Schellenberg GD, Sklar P, State MW,
736 Sutcliffe JS, Walsh CA, Scherer SW, Zwick ME, Barrett JC, Cutler DJ, Roeder K, Devlin B, Daly
737 MJ, Buxbaum JD, Roeder K, Devlin B, Daly MJ, Buxbaum JD. 2014. Synaptic, transcriptional and
738 chromatin genes disrupted in autism. *Nature* **515**:209–215. doi:10.1038/nature13772
739 Deeg KE, Aizenman CD. 2011. Sensory modality-specific homeostatic plasticity in the developing optic
740 tectum. *Nat Neurosci* **14**:548–50. doi:10.1038/nn.2772
741 Eaton BA, Fetter RD, Davis GW. 2002. Dynactin is necessary for synapse stabilization. *Neuron* **34**:729–
742 741. doi:10.1016/S0896-6273(02)00721-3
743 Frank CA, Kennedy MJ, Goold CP, Marek KW, Davis GW. 2006. Mechanisms underlying the rapid
744 induction and sustained expression of synaptic homeostasis. *Neuron* **52**:663–77.
745 doi:10.1016/j.neuron.2006.09.029
746 Frank CA, Pielage J, Davis GW. 2009. A Presynaptic Homeostatic Signaling System Composed of the
747 Eph Receptor, Ephexin, Cdc42, and CaV2.1 Calcium Channels. *Neuron* **61**:556–569.
748 doi:10.1016/j.neuron.2008.12.028
749 Friend SH, Schadt EE. 2014. Clues from the resilient. *Science (80-)* **344**:970–972.
750 doi:10.1126/science.1255648
751 Gaugler T, Klei L, Sanders SJ, Bodea CA, Goldberg AP, Lee AB, Mahajan M, Manaa D, Pawitan Y,
752 Reichert J, Ripke S, Sandin S, Sklar P, Svantesson O, Reichenberg A, Hultman CM, Devlin B,
753 Roeder K, Buxbaum JD. 2014. Most genetic risk for autism resides with common variation. *Nat*

754 *Genet* **46**:881–885. doi:10.1038/ng.3039
755 Genç Ö, Dickman DK, Ma W, Tong A, Fetter RD, Davis GW. 2017. MCTP is an ER-resident calcium
756 sensor that stabilizes synaptic transmission and homeostatic plasticity. *Elife* **6**:e22904.
757 doi:10.7554/eLife.22904
758 Ghobrial G, Araujo L, Jinwala F, Li S, Lee LY. 2018. The Structure and Biological Function of CREG.
759 *Front Cell Dev Biol* **6**:136. doi:10.3389/fcell.2018.00136
760 Gibson G. 2009. Decanalization and the origin of complex disease. *Nat Rev Genet* **10**:134–140.
761 doi:10.1038/nrg2502
762 Gompers AL, Su-Feher L, Ellegood J, Copping NA, Riyadh MA, Stradleigh TW, Pride MC, Schaffler
763 MD, Wade AA, Catta-Preta R, Zdilar I, Louis S, Kaushik G, Mannion BJ, Plajzer-Frick I, Afzal V,
764 Visel A, Pennacchio LA, Dickel DE, Lerch JP, Crawley JN, Zarbalis KS, Silverman JL, Nord AS.
765 2017. Germline Chd8 haploinsufficiency alters brain development in mouse. *Nat Neurosci* **20**:1062–
766 1073. doi:10.1038/nn.4592
767 Harris N, Braiser DJ, Dickman DK, Fetter RD, Tong A, Davis GW. 2015. The Innate Immune Receptor
768 PGRP-LC Controls Presynaptic Homeostatic Plasticity. *Neuron* **88**:1157–64.
769 doi:10.1016/j.neuron.2015.10.049
770 Harris N, Fetter RD, Brasier DJ, Tong A, Davis GW. 2018. Molecular Interface of Neuronal Innate
771 Immunity, Synaptic Vesicle Stabilization, and Presynaptic Homeostatic Plasticity. *Neuron*
772 **100**:1163-1179.e4. doi:10.1016/j.neuron.2018.09.048
773 Hartman JL, Garvik B, Hartwell L. 2001. Principles for the buffering of genetic variation. *Science*
774 **291**:1001–4.
775 Hauswirth AG, Ford KJ, Wang T, Fetter RD, Tong A, Davis GW. 2018. A postsynaptic PI3K-cII
776 dependent signaling controller for presynaptic homeostatic plasticity. *Elife* **7**:e31535.
777 doi:10.7554/eLife.31535
778 Hengen KB, Lambo ME, Van Hooser SD, Katz DB, Turrigiano GG. 2013. Firing Rate Homeostasis in
779 Visual Cortex of Freely Behaving Rodents. *Neuron* **80**:335–342. doi:10.1016/j.neuron.2013.08.038
780 Henry FE, McCartney AJ, Neely R, Perez AS, Carruthers CJL, Stuenkel EL, Inoki K, Sutton MA. 2012.
781 Retrograde Changes in Presynaptic Function Driven by Dendritic mTORC1. *J Neurosci* **32**:17128–
782 17142. doi:10.1523/JNEUROSCI.2149-12.2012
783 Hou J, Tan G, Fink GR, Andrews BJ, Boone C. 2019. Complex modifier landscape underlying genetic
784 background effects. *Proc Natl Acad Sci U S A* **116**:5045–5054. doi:10.1073/pnas.1820915116
785 Iossifov I, O'Roak BJ, Sanders SJ, Ronemus M, Krumm N, Levy D, Stessman HA, Witherspoon KT,
786 Vives L, Patterson KE, Smith JD, Paeper B, Nickerson DA, Dea J, Dong S, Gonzalez LE, Mandell
787 JD, Mane SM, Murtha MT, Sullivan CA, Walker MF, Waqar Z, Wei L, Willsey AJ, Yamrom B,

Lee Y, Grabowska E, Dalkic E, Wang Z, Marks S, Andrews P, Leotta A, Kendall J, Hakker I, Rosenbaum J, Ma B, Rodgers L, Troge J, Narzisi G, Yoon S, Schatz MC, Ye K, McCombie WR, Shendure J, Eichler EE, State MW, Wigler M. 2014. The contribution of de novo coding mutations to autism spectrum disorder. *Nature* **515**:216–221. doi:10.1038/nature13908

Jakawich SK, Nasser HB, Strong MJ, McCartney AJ, Perez AS, Rakesh N, Carruthers CJL, Sutton MA. 2010. Local Presynaptic Activity Gates Homeostatic Changes in Presynaptic Function Driven by Dendritic BDNF Synthesis. *Neuron* **68**:1143–1158. doi:10.1016/j.neuron.2010.11.034

Kim SH, Ryan TA. 2010. CDK5 serves as a major control point in neurotransmitter release. *Neuron* **67**:797–809. doi:10.1016/j.neuron.2010.08.003

Kitano H. 2007. Towards a theory of biological robustness. *Mol Syst Biol* **3**. doi:10.1038/msb4100179

Kowalewski-Nimmerfall E, Schähs P, Maresch D, Rendic D, Krämer H, Mach L. 2014. Drosophila melanogaster cellular repressor of E1A-stimulated genes is a lysosomal protein essential for fly development. *Biochim Biophys Acta - Mol Cell Res* **1843**:2900–2912.

Kulik Y, Jones R, Moughamian AJ, Whippen J, Davis GW. 2019. Dual separable feedback systems govern firing rate homeostasis. *Elife* **8**. doi:10.7554/eLife.45717

Liu G, Tsien RW. 1995. Properties of synaptic transmission at single hippocampal synaptic boutons. *Nature* **375**:404–8. doi:10.1038/375404a0

Loveday C, Tatton-Brown K, Clarke M, Westwood I, Renwick A, Ramsay E, Nemeth A, Campbell J, Joss S, Gardner M, Zachariou A, Elliott A, Ruark E, van Montfort R, Rahman N, Rahman N. 2015. Mutations in the PP2A regulatory subunit B family genes *PPP2R5B* , *PPP2R5C* and *PPP2R5D* cause human overgrowth. *Hum Mol Genet* **24**:4775–4779. doi:10.1093/hmg/ddv182

Maffei A, Fontanini A. 2009. Network homeostasis: a matter of coordination. *Curr Opin Neurobiol* **19**:168–173. doi:10.1016/j.conb.2009.05.012

Mair B, Moffat J, Boone C, Andrews BJ. 2019. Genetic interaction networks in cancer cells. *Curr Opin Genet Dev* **54**:64–72. doi:10.1016/j.gde.2019.03.002

Manning BD, Toker A. 2017. Leading Edge Review AKT/PKB Signaling: Navigating the Network. doi:10.1016/j.cell.2017.04.001

Marder E. 2011. Variability, compensation, and modulation in neurons and circuits. *Proc Natl Acad Sci U S A* 15542–8. doi:10.1073/pnas.1010674108

Marder E, Goaillard J-M. 2006. Variability, compensation and homeostasis in neuron and network function. *Nat Rev Neurosci* **7**:563–574. doi:10.1038/nrn1949

Modabbernia A, Velthorst E, Reichenberg A. 2017. Environmental risk factors for autism: an evidence-based review of systematic reviews and meta-analyses. *Mol Autism* **8**:13. doi:10.1186/s13229-017-0121-4

822 Müller M, Davis GW. 2012. Transsynaptic Control of Presynaptic Ca2+ Influx Achieves Homeostatic
823 Potentiation of Neurotransmitter Release. *Curr Biol*. doi:10.1016/j.cub.2012.04.018
824 Müller M, Genç Ö, Davis GW. 2015. RIM-Binding Protein Links Synaptic Homeostasis to the
825 Stabilization and Replenishment of High Release Probability Vesicles. *Neuron* **85**:1056–1069.
826 doi:10.1016/j.neuron.2015.01.024
827 Müller M, Liu KSY, Sigrist SJ, Davis GW. 2012. RIM controls homeostatic plasticity through
828 modulation of the readily-releasable vesicle pool. *J Neurosci* **32**:16574–85.
829 doi:10.1523/JNEUROSCI.0981-12.2012
830 Mullins C, Fishell G, Tsien RW. 2016. Unifying Views of Autism Spectrum Disorders: A Consideration
831 of Autoregulatory Feedback Loops. *Neuron*. doi:10.1016/j.neuron.2016.02.017
832 Nelson SB, Valakh V. 2015. Excitatory/Inhibitory Balance and Circuit Homeostasis in Autism Spectrum
833 Disorders. *Neuron* **87**:684–698. doi:10.1016/j.neuron.2015.07.033
834 Neuner SM, Heuer SE, Huentelman MJ, O'Connell KMS, Kaczorowski CC. 2019. Harnessing Genetic
835 Complexity to Enhance Translatability of Alzheimer's Disease Mouse Models: A Path toward
836 Precision Medicine. *Neuron* **101**:399-411.e5. doi:10.1016/j.neuron.2018.11.040
837 O'Neil NJ, Bailey ML, Hieter P. 2017. Synthetic lethality and cancer. *Nat Rev Genet* **18**:613–623.
838 doi:10.1038/nrg.2017.47
839 Ortega JM, Genç Ö, Davis GW. 2018. Molecular mechanisms that stabilize short term synaptic plasticity
840 during presynaptic homeostatic plasticity. *Elife* **7**. doi:10.7554/eLife.40385
841 Parrish JZ, Kim CC, Tang L, Bergquist S, Wang T, DeRisi JL, Jan LY, Jan YN, Davis GW. 2014.
842 Krüppel Mediates the Selective Rebalancing of Ion Channel Expression. *Neuron* **82**:537–544.
843 doi:10.1016/j.neuron.2014.03.015
844 Penney J, Tsurudome K, Liao EH, Elazzouzi F, Livingstone M, Gonzalez M, Sonenberg N, Haghighi AP.
845 2012. TOR Is Required for the Retrograde Regulation of Synaptic Homeostasis at the Drosophila
846 Neuromuscular Junction. *Neuron* **74**:166–178. doi:10.1016/j.neuron.2012.01.030
847 Plomp JJ, van Kempen GT, Molenaar PC. 1992. Adaptation of quantal content to decreased postsynaptic
848 sensitivity at single endplates in alpha-bungarotoxin-treated rats. *J Physiol* **458**:487–499.
849 Ramocki MB, Zoghbi HY. 2008. Failure of neuronal homeostasis results in common neuropsychiatric
850 phenotypes. *Nature* **455**:912–918. doi:10.1038/nature07457
851 Sackton TB, Hartl DL. 2016. Genotypic Context and Epistasis in Individuals and Populations. *Cell*.
852 doi:10.1016/j.cell.2016.06.047
853 Sanders SJ, He X, Willsey AJ, Ercan-Sencicek AG, Samocha KE, Cicek AE, Murtha MT, Bal VH,
854 Bishop SL, Dong S, Goldberg AP, Jinlu C, Keaney JF, Klei L, Mandell JD, Moreno-De-Luca D,
855 Poultney CS, Robinson EB, Smith L, Solli-Nowlan T, Su MY, Teran NA, Walker MF, Werling DM,

Beaudet AL, Cantor RM, Fombonne E, Geschwind DH, Grice DE, Lord C, Lowe JK, Mane SM, Martin DM, Morrow EM, Talkowski ME, Sutcliffe JS, Walsh CA, Yu TW, Ledbetter DH, Martin CL, Cook EH, Buxbaum JD, Daly MJ, Devlin B, Roeder K, State MW, State MW. 2015. Insights into Autism Spectrum Disorder Genomic Architecture and Biology from 71 Risk Loci. *Neuron* **87**:1215–1233. doi:10.1016/j.neuron.2015.09.016

Sardi M, Gasch AP. 2018. Genetic background effects in quantitative genetics: gene-by-system interactions. *Curr Genet* **64**:1173–1176. doi:10.1007/s00294-018-0835-7

Shang L, Henderson LB, Cho MT, Petrey DS, Fong C-T, Haude KM, Shur N, Lundberg J, Hauser N, Carmichael J, Innis J, Schuette J, Wu YW, Asaikar S, Pearson M, Folk L, Retterer K, Monaghan KG, Chung WK. 2016. De novo missense variants in PPP2R5D are associated with intellectual disability, macrocephaly, hypotonia, and autism. *Neurogenetics* **17**:43–49. doi:10.1007/s10048-015-0466-9

Simons Simplex Collection – SFARI. n.d.

Spring AM, Brusich DJ, Frank CA. 2016. C-terminal Src Kinase Gates Homeostatic Synaptic Plasticity and Regulates Fasciclin II Expression at the Drosophila Neuromuscular Junction. *PLoS Genet* **12**. doi:10.1371/journal.pgen.1005886

Turrigiano G. 2011. Too many cooks? Intrinsic and synaptic homeostatic mechanisms in cortical circuit refinement. *Annu Rev Neurosci* **34**:89–103. doi:10.1146/annurev-neuro-060909-153238

Velmeshev D, Schirmer L, Jung D, Haeussler M, Perez Y, Mayer S, Bhaduri A, Goyal N, Rowitch DH, Kriegstein AR. 2019. Single-cell genomics identifies cell type-specific molecular changes in autism. *Science* **364**:685–689. doi:10.1126/science.aav8130

Viquez NM, Füger P, Valakh V, Daniels RW, Rasse TM, DiAntonio A. 2009. PP2A and GSK-3beta act antagonistically to regulate active zone development. *J Neurosci* **29**:11484–94. doi:10.1523/JNEUROSCI.5584-08.2009

Viquez NM, Li CR, Wairkar YP, DiAntonio A. 2006. The B' Protein Phosphatase 2A Regulatory Subunit well-rounded Regulates Synaptic Growth and Cytoskeletal Stability at the Drosophila Neuromuscular Junction. *J Neurosci* **26**:9293–9303. doi:10.1523/JNEUROSCI.1740-06.2006

Watt AJ, Desai NS. 2010. Homeostatic Plasticity and STDP: Keeping a Neuron's Cool in a Fluctuating World. *Front Synaptic Neurosci* **2**:5. doi:10.3389/fnsyn.2010.00005

Yang G, Han Y, Tian X, Tao J, Sun M, Kang J, Yan C. 2011. Pattern of expression of the CREG gene and CREG protein in the mouse embryo. *Mol Biol Rep* **38**:2133–2140. doi:10.1007/s11033-010-0340-7

Yeung KS, Tso WWY, Ip JJK, Mak CCY, Leung GKC, Tsang MHY, Ying D, Pei SLC, Lee SL, Yang W, Chung BH-Y. 2017. Identification of mutations in the PI3K-AKT-mTOR signalling pathway in

patients with macrocephaly and developmental delay and/or autism. *Mol Autism* **8**:66. doi:10.1186/s13229-017-0182-4

Yook KJ, Proulx SR, Jorgensen EM. 2001. Rules of Nonallelic Noncomplementation at the Synapse in Caenorhabditis elegans *Genetics* **158**:209 LP – 220.

Zhao C, Dreosti E, Lagnado L. 2011. Homeostatic synaptic plasticity through changes in presynaptic calcium influx. *J Neurosci* **31**:7492–7496. doi:10.1523/JNEUROSCI.6636-10.2011

Acknowledgements

Supported by NINDS Grant (R35-NS097212) and Simons Foundation (SFARI #401636) to GWD and Simons Foundation (SFARI #402281) and NIMH (R01 MH110928) to SJS. We thank Matt State for comments and support and members of the Davis, State and Sanders labs for critical evaluation of the manuscript.

Supplemental Information

Figures S1-S10

Tables S1-S3

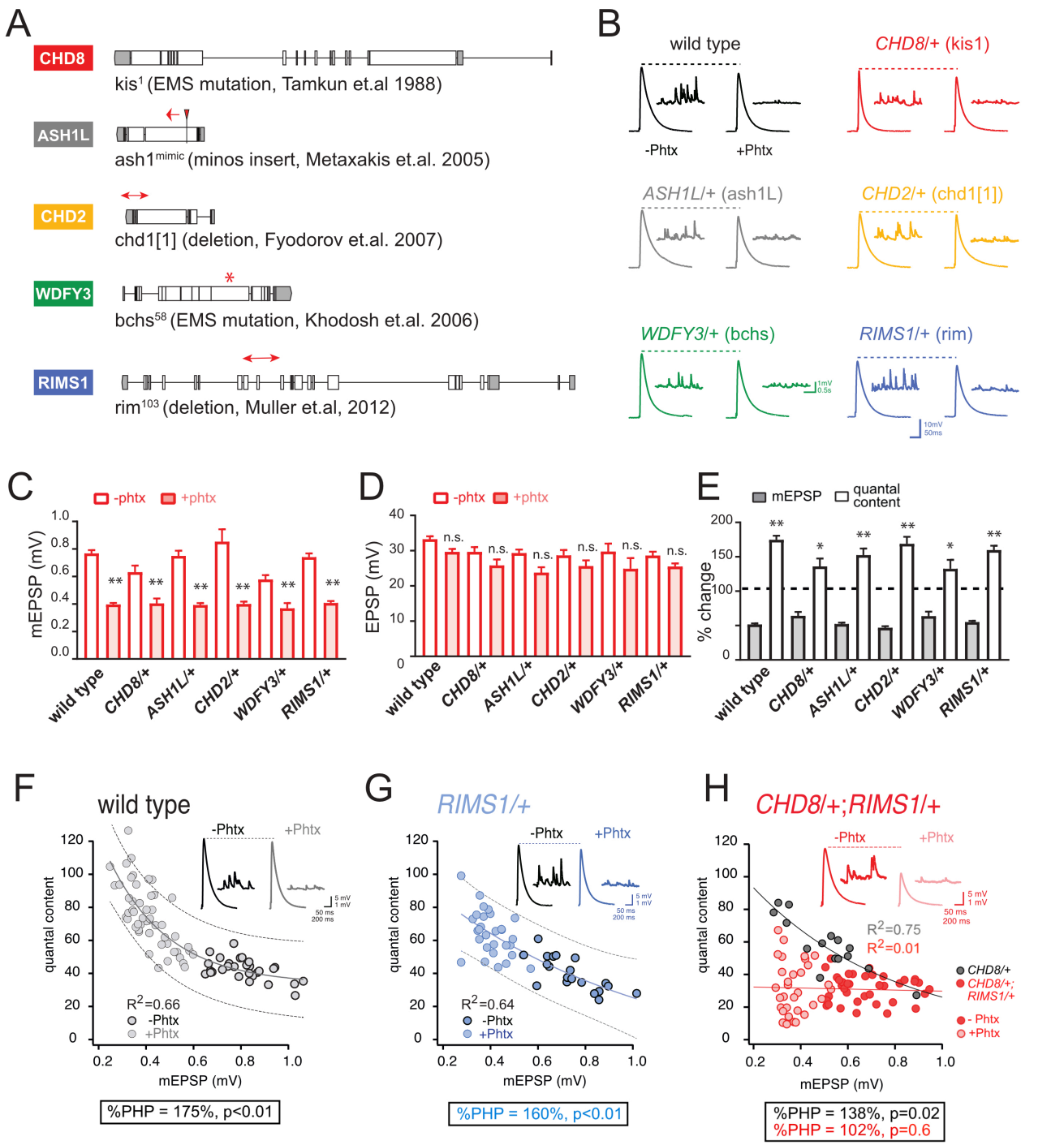

Figure 1: Heterozygous ASD gene mutations do not affect baseline transmission or PHP
A, Schematic of the *Drosophila* locus for *CHD8*, *ASH1L, CHD2*, *WDFY3* and *RIMS1* with gene disruptions indicated. **B,** Representative EPSP and mEPSP traces for indicated genotypes (+/-PhTx for each genotype, left traces and right traces respectively) **C-D,** Quantification of mEPSP amplitude **(C)** and EPSP amplitude **(D)** in the absence and presence of PhTx (open and filled bars respectively). **(E)** The percent change of mEPSP and quantal content as indicated, comparing the presence and absence of PhTx for each genotype with Student's t-test (two tail), * p<0.05, ** p<0.01. Sample sizes for data reported (C-

916 E) are as follows (n reported for each genotype -/+ PhTx): *wild type*: n=36/47; *CHD8/+*: n=7/8;
917 *ASH1L/+*: n=15/25; *WDFY3/+*: n=8/7; *CHD2/+*: n=8/19; *RIMS1/+*: n=20/30. **F-H,** Scatter plots of
918 quantal content (*y* axis) versus mEPSP amplitude (*x* axis) for wild type (left), *RIMS1/+* mutant (middle)
919 and the *CHD8/+; RIMS1/+* double heterozygous mutant. Each symbol represents an individual muscle
920 recording. Inset: representative traces (+/- PhTx). Exponential data fit (black line, R^2-value inset,
921 calculated based on a linear fit). Dashed lines encompass 95% of all data (absent in **(H)** for clarity).
922 Below each graph (F-H), boxes display percent PHP (+/- PhTx for each genotype), statistical values
923 compared to baseline (H).
924

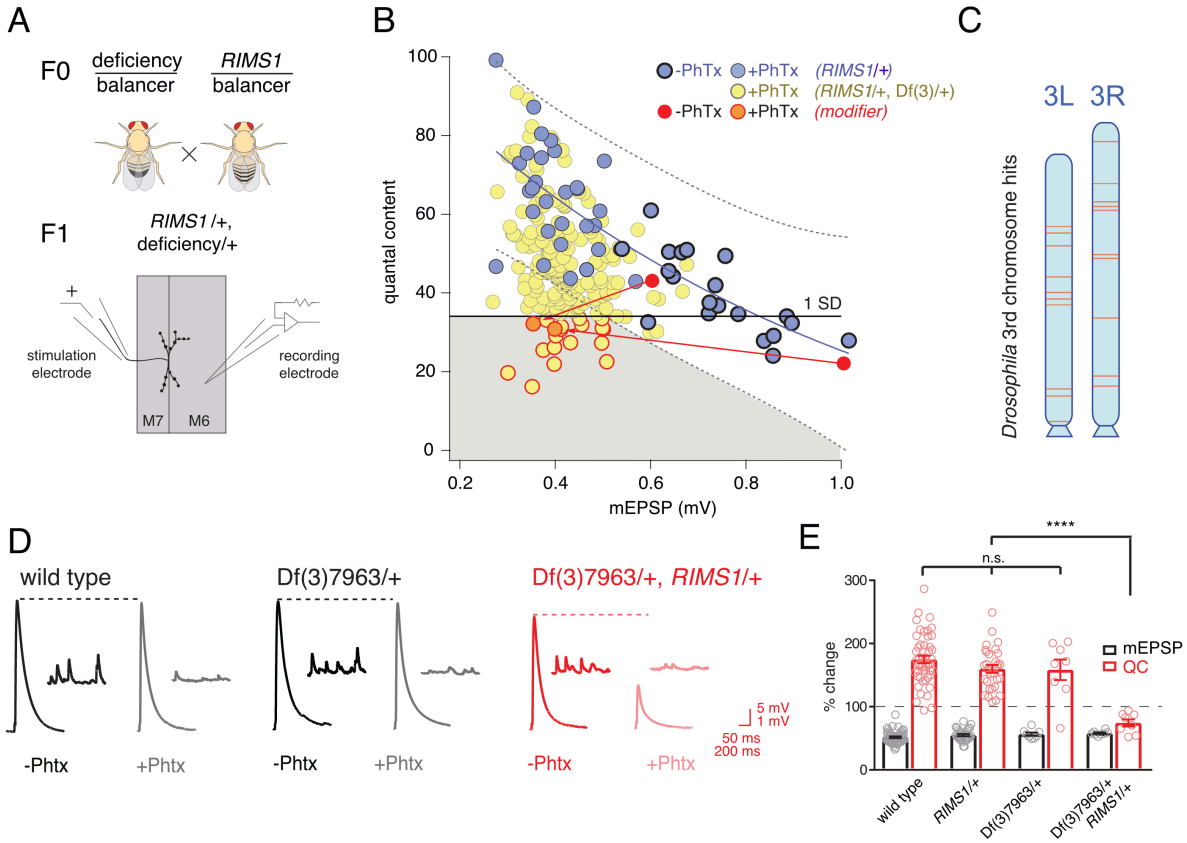

Figure 2: Screen for common genomic modifiers of ASD-associated gene mutations.
A, Diagram of genetic screen. **B,** Screen results are shown with yellow circles representing average data per genotype. Fit (solid blue line) and confidence interval (dotted lines encompassing 95% of all data) from *RIMS1/+* are overlaid. Black horizontal line defines one standard deviation from population mean (yellow circles). Gray area encompasses potential hits residing outside the *RIMS1/+* confidence interval and below the solid line. Two modifiers are shown in the absence (dark red circles) and presence of PhTx (light red circles, dark outline) **C,** Approximate location of hits (red lines) on chromosome 3. **D,** Representative traces for indicated genotypes in the presence and absence of PhTx as indicated. **E,** Average percent change in mEPSP amplitude (gray bars) and quantal content (red bars) in presence of PhTx compared to baseline. One-way ANOVA and posthoc Tukey's multiple comparisons; **** $p<0.0001$ for quantal content (QC).

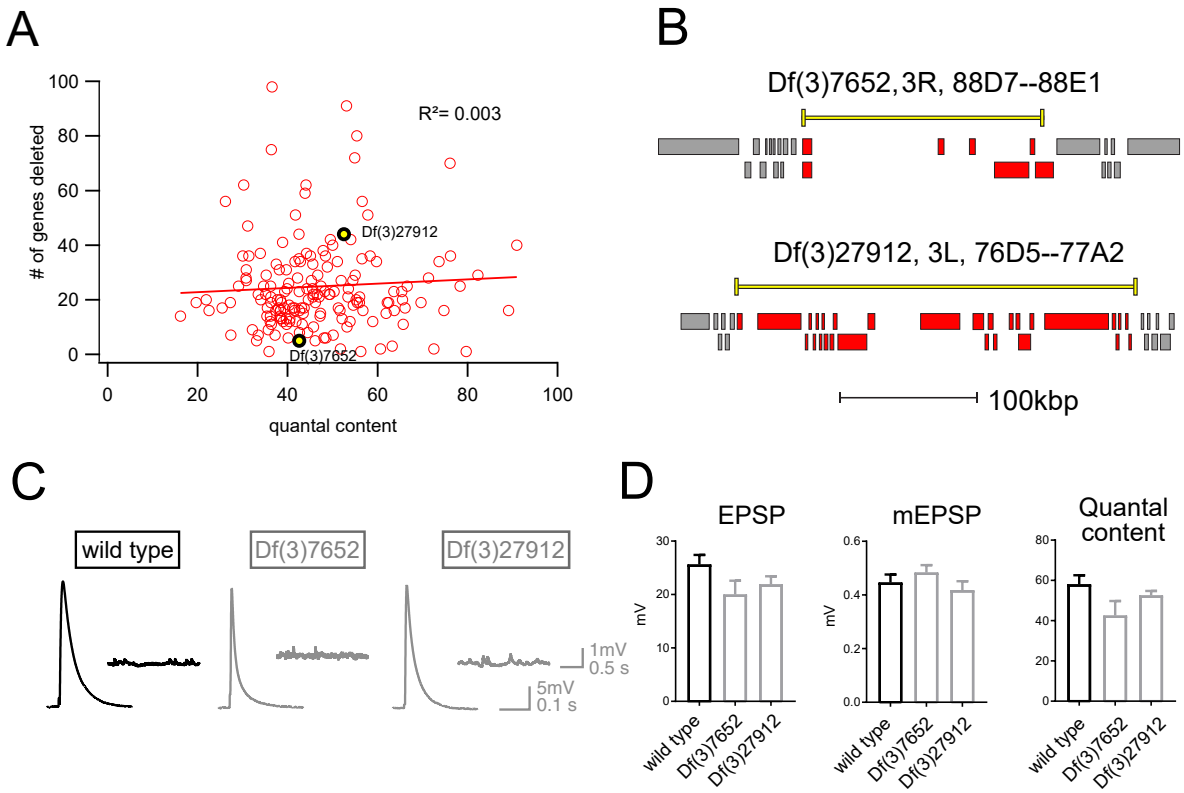

Figure 3: Absence of an additive effect of gene heterozygosity on synaptic transmission or PHP
A, Scatter plot showing the number of genes deleted (*y* axis) versus quantal content (*x* axis) in the presence of PhTx for all deficiencies tested. Each circle represents average data from an individual muscle recording for an individual deficiency. Red line shows the fit with a Pearson coefficient of 0.003. **B,** Schematic of two deficiency alleles showing the extent of the deletion (yellow bars) and the genes deleted (red boxes) **C,** Representative EPSP and mEPSP traces for indicated genotypes **D,** Quantification of EPSP, mEPSP amplitude and quantal content for the indicated genotypes. All deficiencies recorded as heterozygous mutations in the presence of *RIMS1*/+)

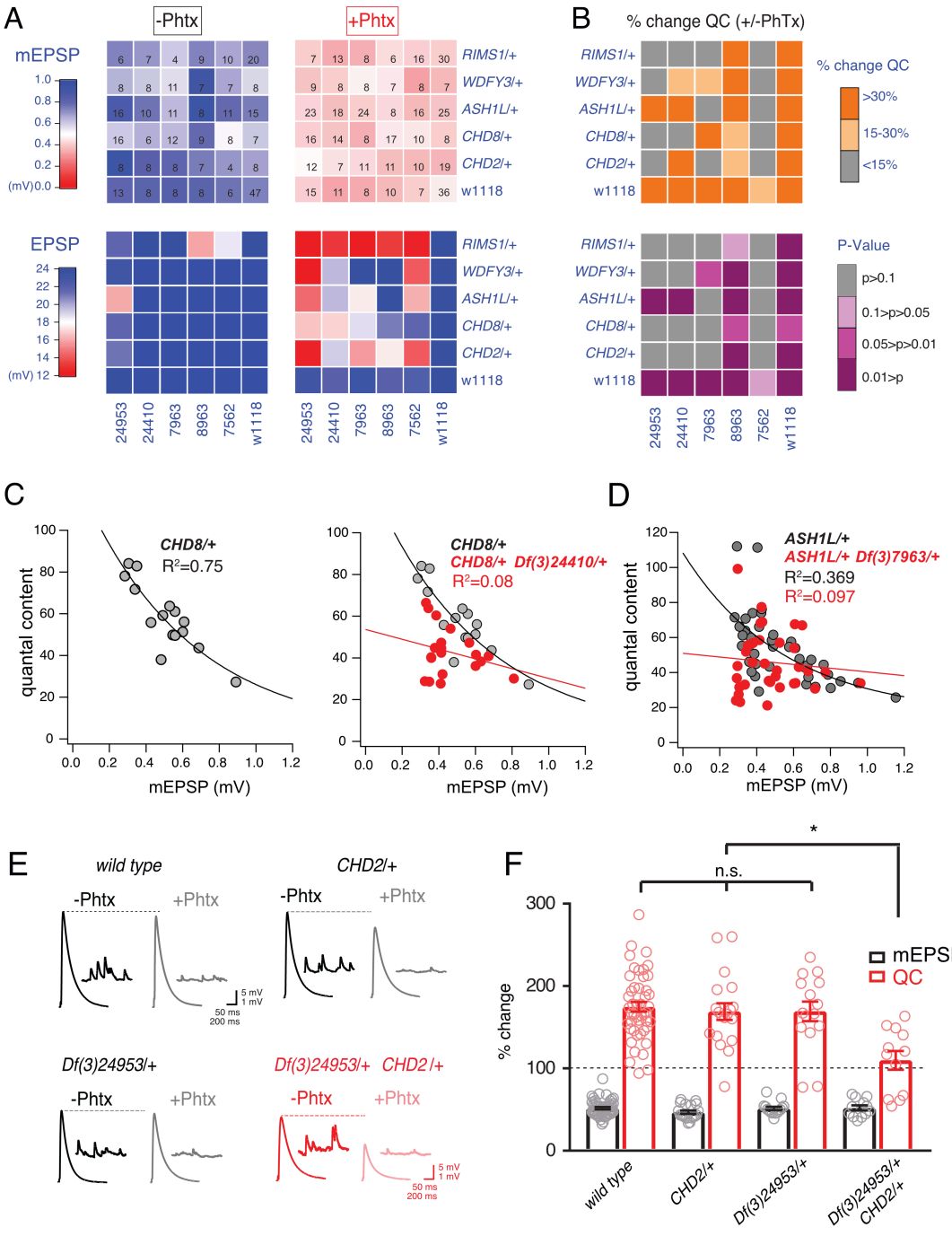

Figure 4: Identification of common modifiers of diverse ASD-associated mutations.
A, Genetic interaction matrix showing average mEPSP (top two matrix) and EPSP (bottom two matrix) amplitudes in the absence (left) and presence (right) of PhTx, as indicated. Values are according to lookup codes at left. Each individual box represents average data for a double-heterozygous mutant at intersection of x and y axes. Sample size (number of NMJ recordings) is displayed for each box (top) and are identical below (bottom). **B,** Top matrix (orange and gray) is organized as in (a). Average percent change in quantal content (+ PhTx) compared to baseline (- PhTx), values according to lookup code**.** Bottom panel, shows data from top panel re-plotted diagramming p-values for the observed percent change in quantal content (+/-PhTx), values according to lookup code. Student's t-test (two tail)

961 comparing each genotype +/- PhTx. **C,** Scatter plots of quantal content (*y* axis) versus mEPSP amplitude
962 (*x* axis) for *CHD8*/+ (left), and *CHD8/+;Df(3)24410/+*. **D** Scatter plot as in (c) for *ASH1L*/+ and
963 *ASH1L*/+, /*Df(3)7963*/+. Each dot represents average data from an individual muscle recording. Fits as
964 indicated. R^2 values as indicated (calculated based on linear fit). **E,** Representative traces for indicated
965 genotypes (+/-PhTx) **F,** Percent change in mEPSP (gray bars) and quantal content (red bars) in presence
966 of PhTx compared to baseline. One-way ANOVA and posthoc Tukey's multiple comparisons ; * $p<0.05$.
967

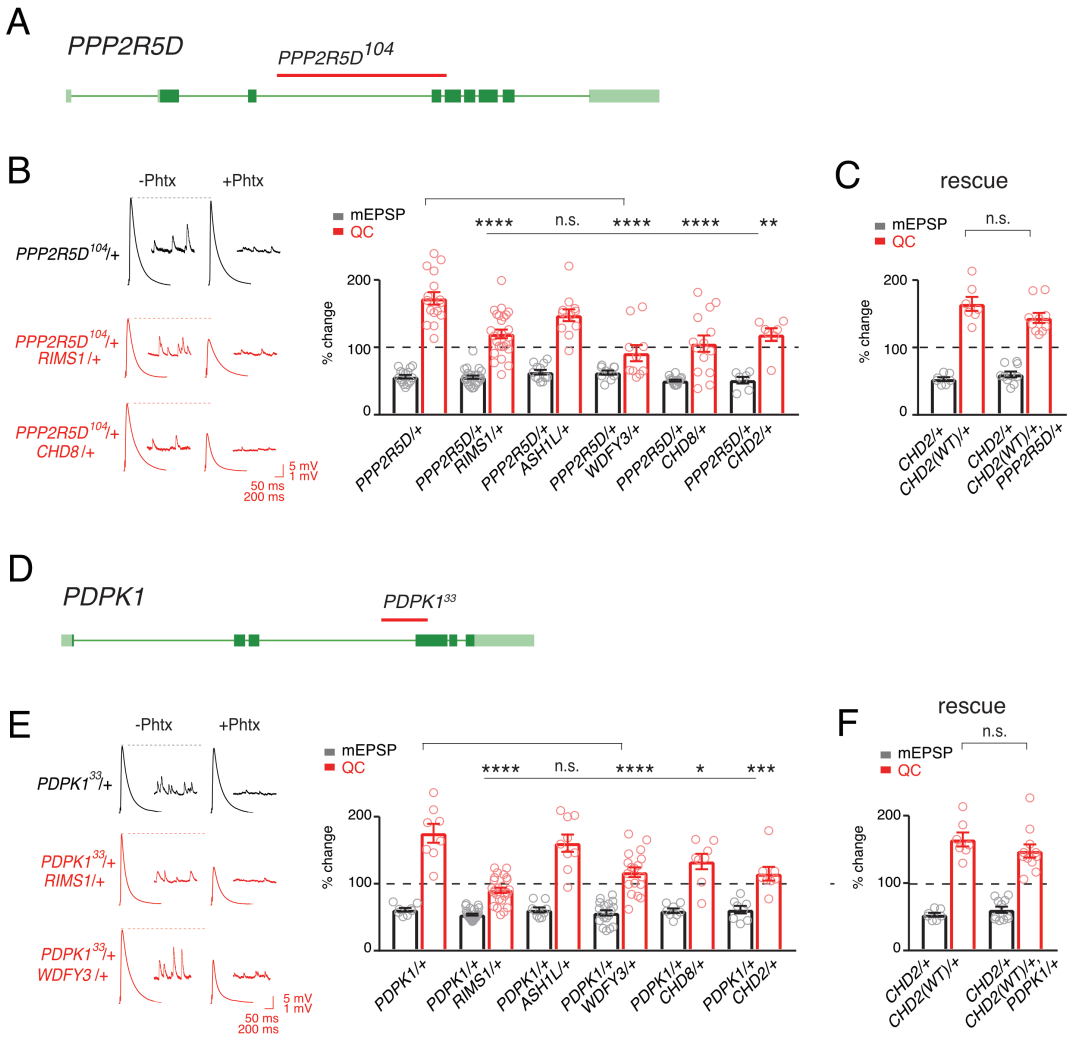

Figure 5: Single genes are common modifiers of diverse ASD-associated mutations.
A, Schematic of the *PPP2R5D* gene locus and the *PPP2R5D*^{104} deletion mutation (red horizontal bar). **B,** Representative traces for indicated genotypes. Bar graph (right) shows percent change in mEPSP (gray) and quantal content (red) (+/- PhTx). **C,** Data as in **B** for rescue of the double heterozygous *CHD2*/+ and *PPP2R5D*^{104}/+ mutant by incorporation of a *CHD2* translocation (*CHD2*^{WT}/+). **D,** Schematic of the *PDPK1* gene locus with the *PDPK1*^{33} deletion mutation (red horizontal bar). **E,** Representative traces for indicated genotypes. Bar graph (right) as in **B**. **F,** Data as in **C** for the genomic rescue of double heterozygous *CHD2*/+ and *PDPK1*^{33}/+ mutants. One-way ANOVA, Dunnett's multiple comparisons * $p<0.05$, ** $p<0.01$, *** $p<0.001$, **** $p<0.0001$ for **B** and **E**, Student's t-test, two-tailed for **C** and **F**, n.s. $p>0.05$).

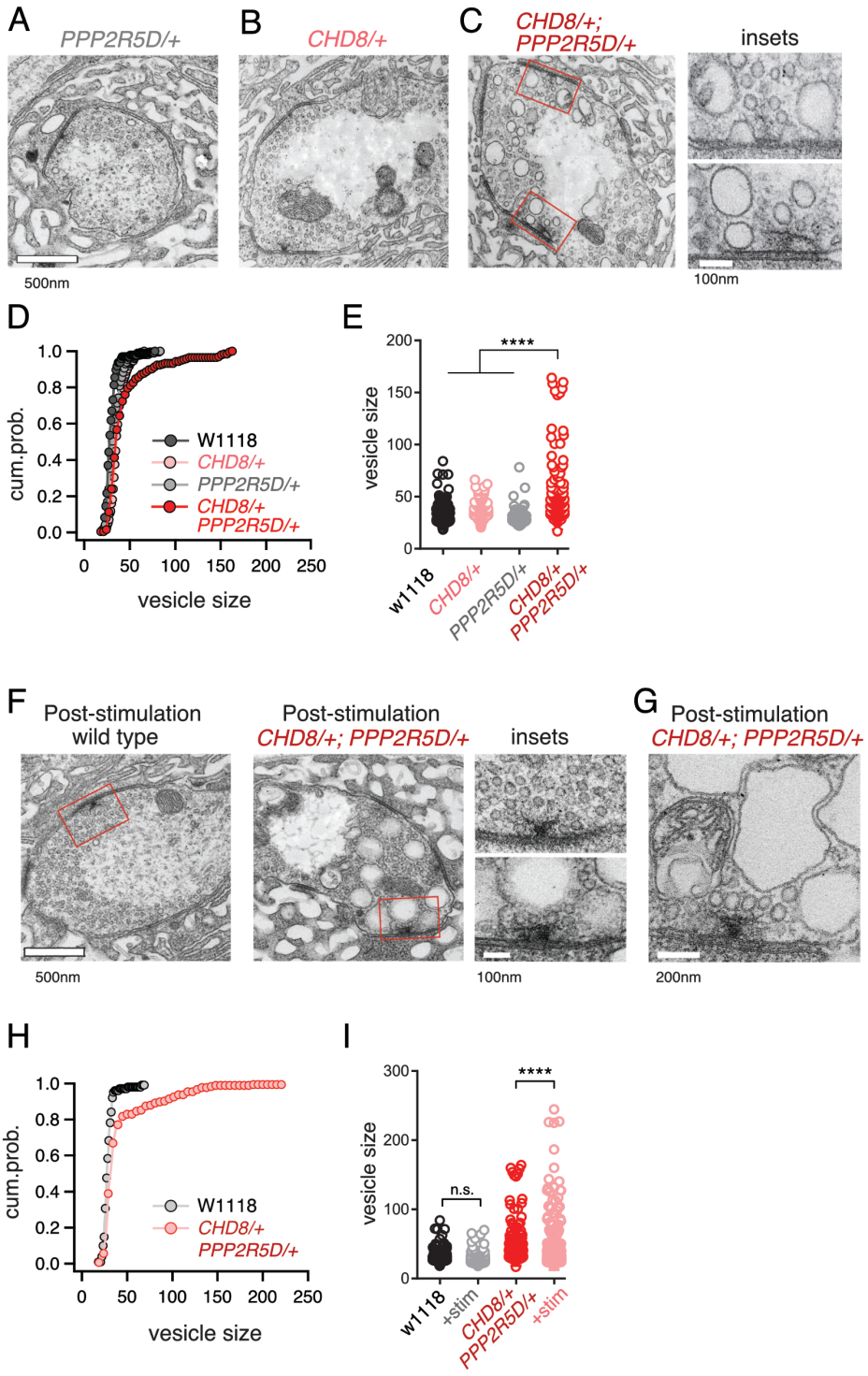

Figure 6: ASD gene-modifier interaction causes impaired synaptic membrane organization
A-C, Representative electron microscopy images of individual boutons inclusive of (**A**) *PPP2R5D/+*, (**B**) *CHD8/+* and (**C**) *CHD8/+*; *PPP2R5D/+* double heterozygous mutant. Insets **(C)** show individual active zones taken from the image on the left (red rectangles) **D,** Cumulative probability distribution of the vesicle size for wild type (*w1118*) and *CHD8/+* and *PPP2R5D/+* single mutants, as well as the *CHD8/+*; *PPP2R5D/+* double heterozygous mutants. Each point reflects the average at a single active zone. **E,** Plot

of individual data points for each genotype as shown in (**D)**. **F,** Representative electron microscopy images for individual boutons for indicated genotypes after stimulation with 50 Hz for 10 seconds and rapid fixation. Insets show active zones for *wild type* (top) and the *CHD8*/+; *PPP2R5D*/+ double heterozygous mutant (bottom) taken from the images on the left (red rectangles) **G,** An example image from the *CHD8*/+; *PPP2R5D*+ double heterozygous mutant with larger vesicles having a crenulated appearance after stimulation **H,** Cumulative probability distribution of the vesicle size for wild type (*w1118*) and the double heterozygous mutant *CHD8*/+; *PPP2R5D*/+ after stimulation and rapid fixation. Each point reflects the average at a single active zone. **I,** Plot of individual data points for data in (H). One-way ANOVA Tukey's multiple comparisons, **** $p<0.001$, n.s. $p>0.05$.

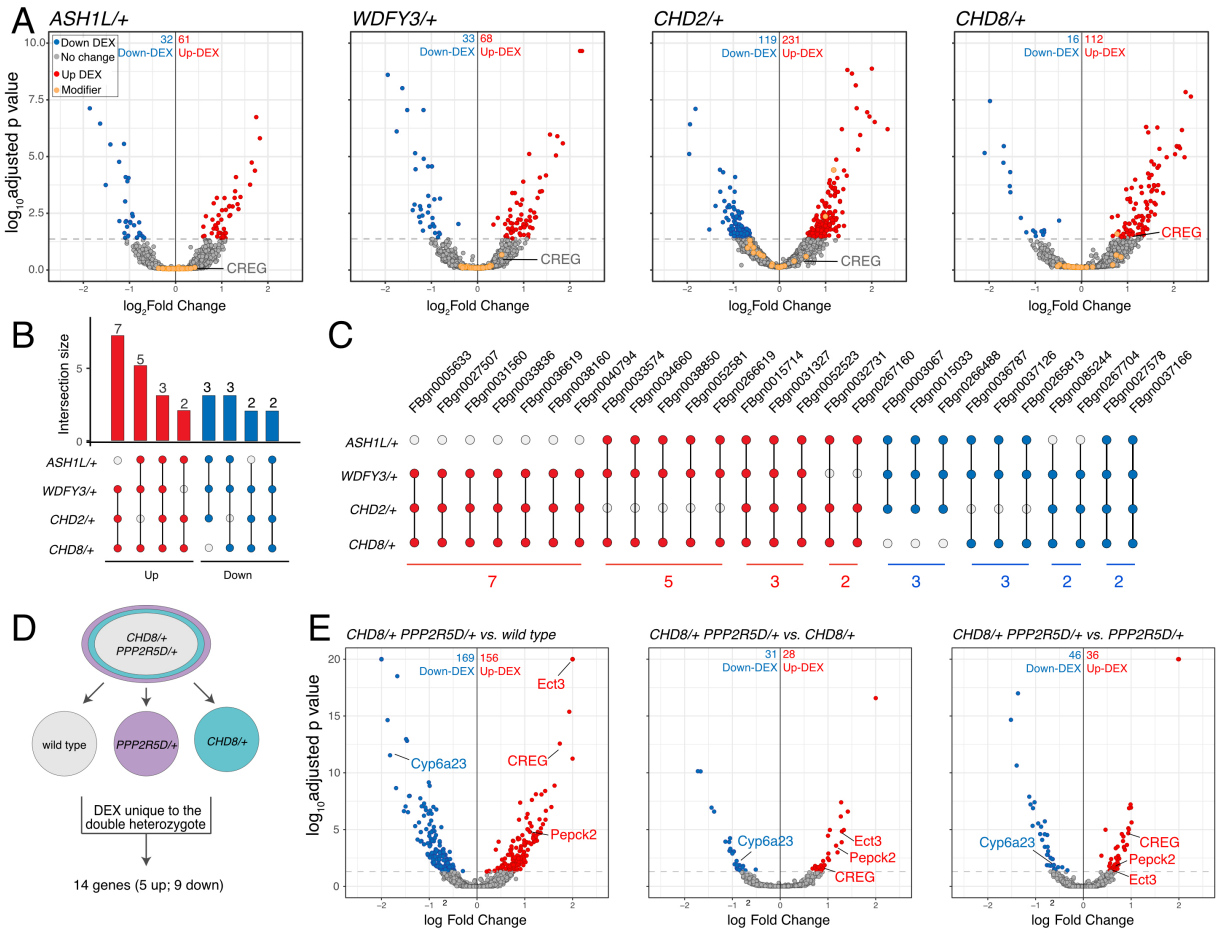

Figure 7: Differential gene expression analysis identifies *CREG*.
A, Volcano plot display of differentially expressed genes (DEX) for each heterozygous mutant versus wild type. Candidate ASD-gene modifiers are indicated (orange dots). Horizontal dashed line indicates cutoff of adjusted p-values (0.05). **B,** Matrix shows all intersections of DEXs from the four indicated genotypes (see Database S1). Filled circles in the matrix indicate sets that are part of the intersection between genotypes. Bar graphs on the top show the total number of DEXs for each set, ordered by the size of intersection. (blue, up-regulated; red, down-regulated). **C,** Individual genes are listed at the intersection of each genotypes. **D,** Schematic showing the selection of 14 genes uniquely dysregulated in *CHD8/+; PPP2R5D/+* double heterozygous mutants. **E,** Volcano plot display of DEX calculated as *CHD8*/+; *PPP2R5D*/+ versus wild-type, *CHD8*/+; *PPP2R5D*/+ versus *CHD8*/+ and *CHD8*/+; *PPP2R5D*/+ double heterozygotes versus *PPP2R5D*/+ alone.

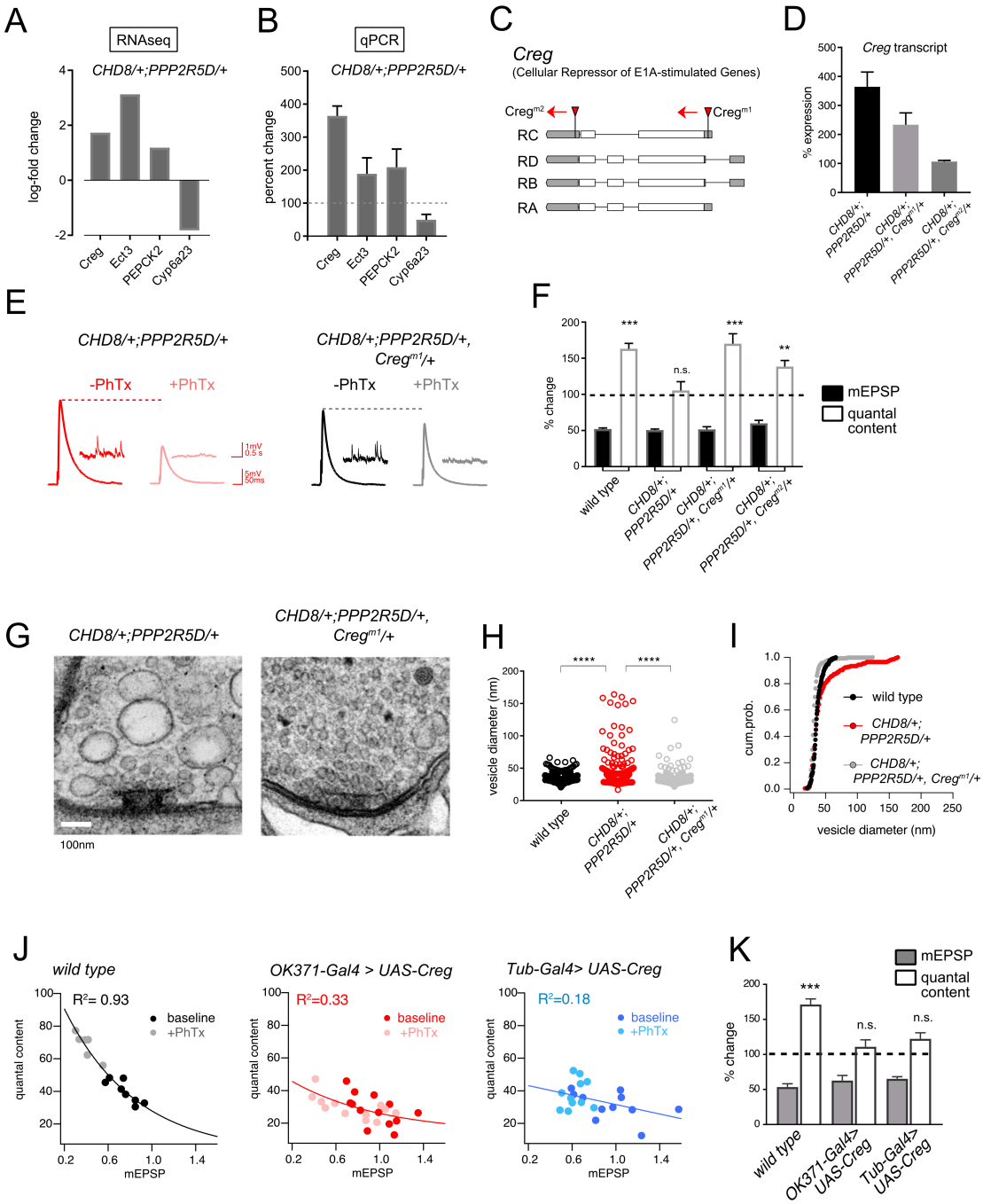

1017
1018
1019 **Figure 8: *CREG* is a homeostatic repressor that blocks PHP and regulates synapse ultrastructure.**
1020 **A,** Quantification of transcriptional changes calculated by RNAseq for four genes (*CREG*, *Ect3*, *PEPCK2*
1021 and *Cyp6a23*) in *CHD8*/+; *PPP2R5D*/+ double heterozygous mutant versus wild-type. **B,** Quantification
1022 of the transcriptional changes for the same genes in (**B)** by qPCR. **C,** Schematic of the *Drosophila CREG*
1023 locus. The positions of two transposon insertion mutations are shown (red triangles). **D,** Average *CREG*
1024 transcript levels calculated by qPCR are shown for the indicated genotypes **E,** Representative EPSP and
1025 mEPSP traces for indicated genotypes. **F**, Bar graph (right) shows percent change in mEPSP (black filled)

and quantal content (no fill) (+/- PhTx). **G,** Representative electron microscopy images of individual active zones from indicated genotypes (double heterozygous mutant at left, triple heterozygous mutant at right). Scale bar:100nm. **H,** Individual data points shown for indicated genotypes. **I,** Cumulative probability distribution of the vesicle size for the genotypes shown in (H). **J,** Scatter plots of quantal content (*y* axis) versus mEPSP amplitude (*x* axis) for *wild type* (left), *OK371-Gal4>UAS-Creg* (middle, red) and *Tub-Gal4>UAS-Creg* (right, blue). Fits as indicated. R^2 values as indicated (calculated based on linear fit). **K,** Percent change in mEPSP (gray bars) and quantal content (red bars) in presence of PhTx compared to baseline. n.s. $p>0.05$, ** $p<0.01$, *** $p<0.001$, **** $p<0.0001$.

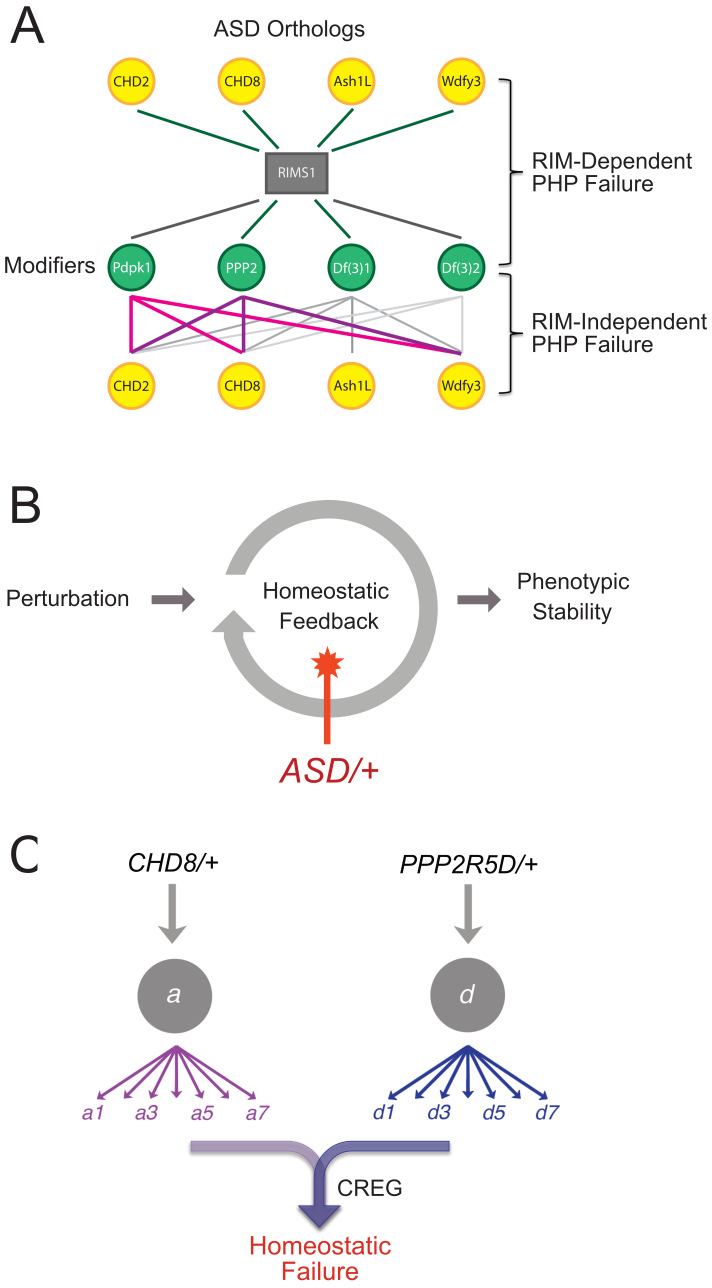

Figure 9: Summary and Model

A, Summary of genetic interactions. *RIMS1* interacts with three of four ASD gene orthologues, impairing PHP. *RIMS1* interactions identified in a genetic screen as modifiers are shown below in green. Each modifier interacts with multiple ASD heterozygous mutations in a RIM independent manner, disrupting PHP. The data present a complex network of gene-gene interactions (yellow and green) that diminish the robustness of PHP. **B,** Homeostatic signaling systems robustly ensure stable neural function. However, the homeostatic signaling system itself is sensitive to genetic perturbation. We demonstrate that PHP is sensitive to mutations in multiple genes that were identified as ASD risk factors. In at least one instance, this is due to the up-regulation of a PHP interfering factor (*CREG*) and the red star indicates this a possible mechanisms more generally. **C,** Complexity of interpreting double heterozygous gene-gene

interactions. Signaling systems are not blocked by heterozygous gene mutations, but are likely to be attenuated to some degree. The combined effect of two higher-order heterozygous gene mutations creates a downstream, intersectional effect that is very difficult to predict. In the case of this paper, we succeeded in identifying a novel intersection causing up-regulation of *CREG*, which disrupts the homeostatic signaling system.

Methods

Fly Stocks

All *Drosophila* stocks were kept and raised on standard food at 25 °C. *RIMS1* was previously described (Sigrist, 2012). *PPP2R5D* was a gift from Dr. Aaron Diantonio. *Chd2[1]* and *Chd2[1],Chd2*^{wt} flies were gifts from Dr. Alexandra Lusser and Dr. Dmitry Fyodorov. All other *Drosophila* stocks were obtained from the Bloomington Drosophila Stock Center unless otherwise noted. *W1118* is used as wild-type controls. 3rd chromosome deficiency fly stocks are balanced over *TM6b* and all stock are on the *W1118* background.

Molecular biology:

Drosophila CREG cDNA was obtained by amplifying the single open reading frame from genomic DNA by PCR and cloning directly in to the pENTR vector (Gateway Technology; Invitrogen). We engineered a CACC site in the forward primer for the subsequent Gateway reaction: forward primer for pUASt-creg: 5′ CACCATGGATTCGGACAGCACC 3′; reverse primer for pUASt-creg with a stop codon, 5′ TCA ATT CGA AAC AGC GTA ATA 3′. The final construct were sequenced to ensure there were no mutations. The creg cDNA was then cloned into proper destination vector obtained from the Drosophila Gateway Vector Collection (Carnegie Institution, DGRC barcode #1129). Transgenic lines were generated and mapped using standard methods.

Electrophysiology

All current clamp recordings were performed from muscle six, at the second and third segment of the third-instar *Drosophila* with an Axoclamp 900 amplifier (Molecular Devices). The composition of the extracellular solution (HL3) is (in mM) 70 NaCl, 5 KCl, 10 $MgCl_2$, 10 $NaHCO_3$, 115 sucrose, 4.2 trehalose, 5 HEPES. Ca^{2+} concentration in the extracellular solution is 0.35 mM unless otherwise noted. Homeostatic plasticity was induced by incubating the larvae with Philantotoxin-433 (PhTx, 15–20 µM, Sigma) for 10 min as previously described (Frank et al., 2006; Genç et al., 2017). Quantal content calculation is made by dividing average EPSP to mEPSP. mEPSPs were analyzed with MiniAnalysis program (Synaptosoft). All other physiology data were analyzed with custom written functions in Igor 6 (Wavemetrics Inc). Data collected from a minimum of two animals from two independent crosses.

Immunohistochemistry

Third-instar larvae were dissected, fixed in Bouin's fixative or 4% PFA in PBS, and immunostained with previously described methods (Eaton et al., 2002; Harris et al., 2015). Third instar larvae were dissected with cold HL3 and immediately fixed with PFA (4%) and incubated overnight at 4 C with

primary antibodies (rabbit anti-Dlg, 1:1000; anti-Brp 1:100, Life Technologies). Alexa-conjugated secondary antibodies were used for secondary staining (Jackson Laboratories 1:500). An inverted epifluorescence deconvolution confocal microscope (Axiovert 200, Zeiss) equipped with a 100X objective (N.A. 1.4), cooled CCD camera (CoolSnap HQ, Roper Scientific) was used to acquire images. All acquisition, deconvolution and analysis were done by Slidebook 5.0 software (3I, Intelligent Imaging). Structured illumination microscopy (Nikon LSM 710 equipped with 63X objective and Andor Ixon EMCCD camera) was used to perform Brp puncta and Dlg labeling experiments. Bouton numbers were quantified as described previously (Harris et al., 2015).

RNA extraction and library preparation for RNA sequencing

RNA was extracted from the adult heads (5-7 days post-pupation) of heterozygous mutants of four genotypes (*ASH1L*/+ and *WDFY3*/+ and *CHD2*/+ and *CHD8*/+) and wild types with four biological replicates per group by using Lexogen's RNA Extraction Kit (Lexogen). RNA quality was checked with Bioanalyzer (Agilent Technologies Inc.) prior to library amplification. 3'mRNA-Seq Library Prep Kit for Illumina (FWD) from Lexogen was used for first strand cDNA, second strand synthesis, dsDNA purification, i7 single indexing, library amplification and final library purification. To estimate the PCR cycle numbers for library amplification, qPCR was done by using PCR Add-On Kit (Lexogen). Purified final libraries were quality tested by using Agilent Bioanalyzer 2100 with High Sensitivity DNA chips (Agilent Technologies Inc.). Qubit fluorometer (ThermoFisher Scientific) was used to quantify the concentration of the final library. Barcoded libraries are then sequenced using an Illumina HiSeq 4000 at 50bp single-end reads in the CAT genomic facility at UCSF. There was a median of 14.3 million (M) mapped reads per sample (interquartile range, IQR: 8.0M-20.6M).

Read mapping and quantification of gene expression

Read count and transcript per million reads mapped (TPM) were determined using Salmon software version 0.12.0. A reference genome index for Salmon was created according to developer's instructions for the Drosophila Melanogaster genome BDGP6 (Ensembl v92). Reads mapping and quantitation was simultaneously performed to individual transcripts.

Differential expression across heterozygous mutant flies

Differential expression of heterozygous mutant flies was determined by pooling samples from the same genotype. Gene expression profiles between mutant and wild type were collated using the R package tximport (version 1.6.0). The R package DESeq2 (version 1.18.1) used raw gene counts to determine differentially expressed genes (DEGs) by genotype with the linear model [Gene counts ~ Batch

+ Genotypes]. Protein coding and lincRNA genes defined by the BDGP6 were included in differential expression. Expression was adjusted for batch to account for difference between fly lines, tissue source, and library preparation. The p-values were adjusted for Benjamini-Hochberg Procedure through DESeq2 with a target alpha = 0.1, and genes were considered DEGs at FDR<0.05 and ±50% expression changes.

Single cell Patch-seq

To obtain the cytoplasmic content of the cell, we performed whole-cell tight-seal patch clamp in motoneurons expressing GFP (Kulik et al., 2019). We established whole-cell configuration with leak currents less than 100pA. We gently sucked the cytoplasmic content of the cell by applying a negative pressure to the patch-pipette. Then, we pulled the individual motoneuron from the tissue while visually confirming the GFP fluorescent signal at the tip of the pipette. Immediately after, we immersed the pipette tip in a test tube containing the Cell Lysis Buffer and RNAse inhibitor medium and broke the pipette tip by gently touching to the tube wall. The content of the pipette tip was ejected by applying positive pressure. We pooled 4-8 motoneurons for one reaction.

We used the Low Input RNA: cDNA Synthesis, Amplification and Library Generation kit from NEB (New England Biolabs Inc.) to isolate, reverse-transcribe the RNA and prepare the libraries for sequencing. Following the reverse transcription and template switching, we amplified the cDNA by PCR. Amplified cDNA was cleaned up by using SPRI beads. The quality and quantity of the amplified cDNA was assessed by Bioanalyzer (Agilent Technologies Inc.). After fragmentation and adaptor ligation, adaptor-ligated DNA were enriched with i7 primer and universal primer by PCR-amplification. Amplified libraries were quality checked by Biolanalyzer with High Sensitivity DNA chips (Agilent Technologies Inc.) and the quantity was measured by Qubit fluorometer (ThermoFisher Scientific). Barcoded libraries were sequenced using an Illumina HiSeq 4000 at 100bp paired-end reads in the CAT genomic facility at UCSF.

Patch-seq transcriptional analysis

Raw reads were first processed with flexbar version 3.5.0 (https://github.com/seqan/flexbar) to remove adapters specific to the NEBNext library prep, using parameters as described in https://github.com/nebiolabs/nebnext-single-cell-rna-seq. The reads were then processed with HTStream v.1.1.0 (https://ibest.github.io/HTStream/) to perform data QA/QC, remove Illumina adapter contamination, PCR duplicates, and low-quality bases/sequences.

The trimmed reads were aligned to the Drosophila melonogaster genome v.BDGP6.22 (http://ensembl.org/Drosophila_melanogaster/Info/Annotation) with annotation release version 98 using the aligner STAR v. 2.7.0e (Dobin, et al. 2013, Reference at

https://www.ncbi.nlm.nih.gov/pubmed/23104886) to generate raw counts per gene. On average, 93.7% of the trimmed reads aligned to the Drosophila genome, and 80% of the trimmed reads uniquely aligned to an annotated Drosophila gene.

Differential expression analyses were conducted using limma-voom in R (limma version 3.40.6, edgeR version 3.26.7, R 3.6.1). Prior to analysis, genes with fewer than 5 counts per million reads in all samples were filtered, leaving 8598 genes. The differential expression analysis was conducted independently for the two experiments represented in the samples.

qPCR

RNA was extracted from third-instar larval CNS or adult heads (5-7 days post-pupation) with RNeasy Plus Micro kit (Qiagen). RNA isolation was followed with DNase digestion with Turbo DNA-free (Ambion). For the first strand synthesis Super Script II RT was used (Invitrogen). Taqman Fast Universal PCR solution was mixed with TaqMan probe with an Applied Biosystems FAM dye. RPL32 was amplified as an internal control. Expression fold-changes are quantified by ddCT method. Data represent three biological and three technical replicates.

Electron Microscopy

Electron microscopy experiments were performed as previously described (Harris et al., 2015). For high-frequency stimulation experiments, larval fillet preparations were fixed immediately (1-5 seconds) following stimulation. Data are acquired from at least two animals.

Statistical analysis of physiology and morphology data

Average values are presented as mean ± standard error of mean. All statistical tests are indicated in the figure legends, referring to individual panels within the figure. For multiple comparisons, we used one-way ANOVA, followed by Dunnett's or Tukey multiple comparisons. To test the difference between two groups, we used unpaired two-tailed Student's t-test. Pearson correlation coefficients were calculated following a linear-fit of the X-Y (quantal size vs. quantal content) data, although supra-linear best-fits are sometimes displayed, purely for the purpose of display.

1185 **Supplemental Information**

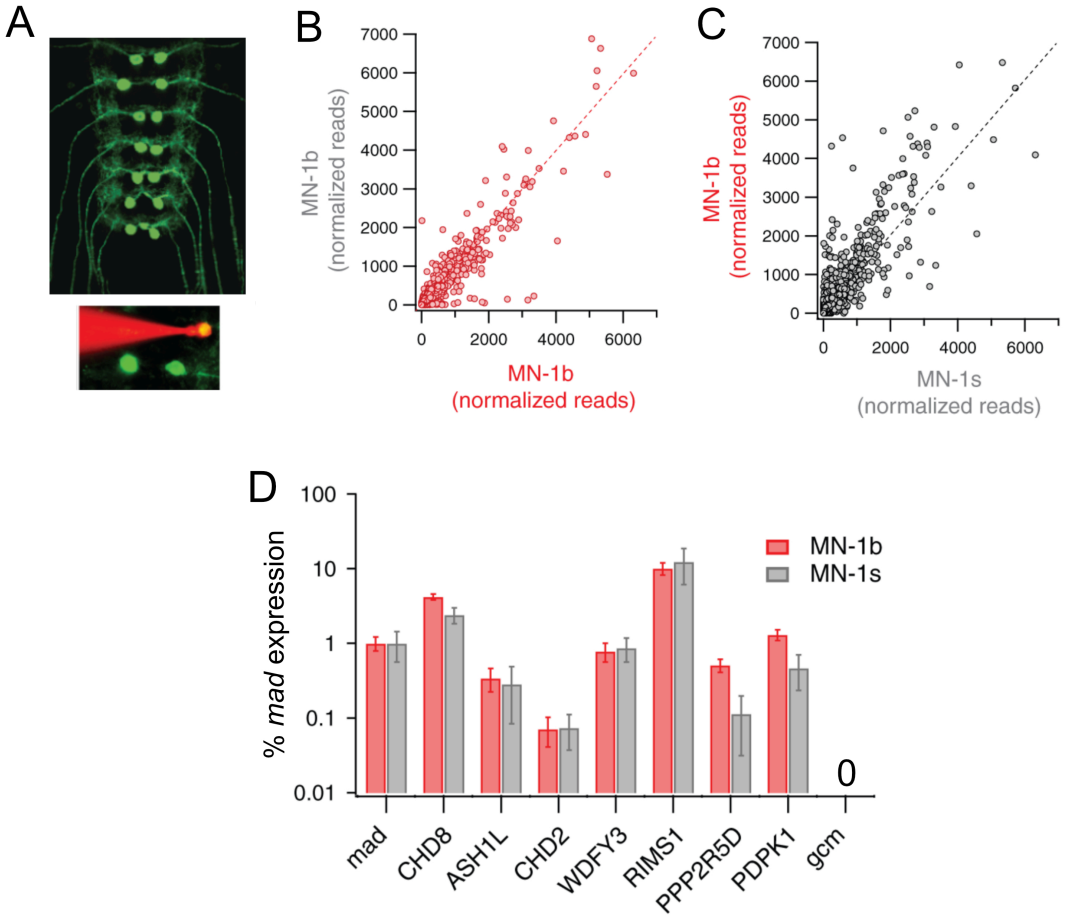

1186
1187
1188
1189 **Figure S1: Patch-Seq analysis of gene expression in type 1b and type 1s motoneurons.**
1190 **A,** Image of the larval central nervous system with expression of *UAS-CD8-GFP* driven by *MN1-GAL4*.
1191 Inset, a rhodamine filled patch electrode targets a single identified motoneuron for excision and
1192 sequencing (see methods). **B,** Differential gene expression analysis for two different experiments
1193 comparing MN1b (3 biological replicates each). Most data rely on unity as expected. **C,** Comparison of
1194 gene expression for type 1b and type 1s motoneurons. **D,** Expression analysis of ASD gene orthologs in
1195 type 1b and type 1s motoneurons in the third larval instar taken from the patch seq data. Expression is
1196 normalized to the well-established, motoneuron-expressed transcription factor *mothers against*
1197 *decapentaplegic* (*mad*). As confirmation of predicted gene expression we note the absence of expression
1198 for *glial cells missing* (*gcm*).
1199

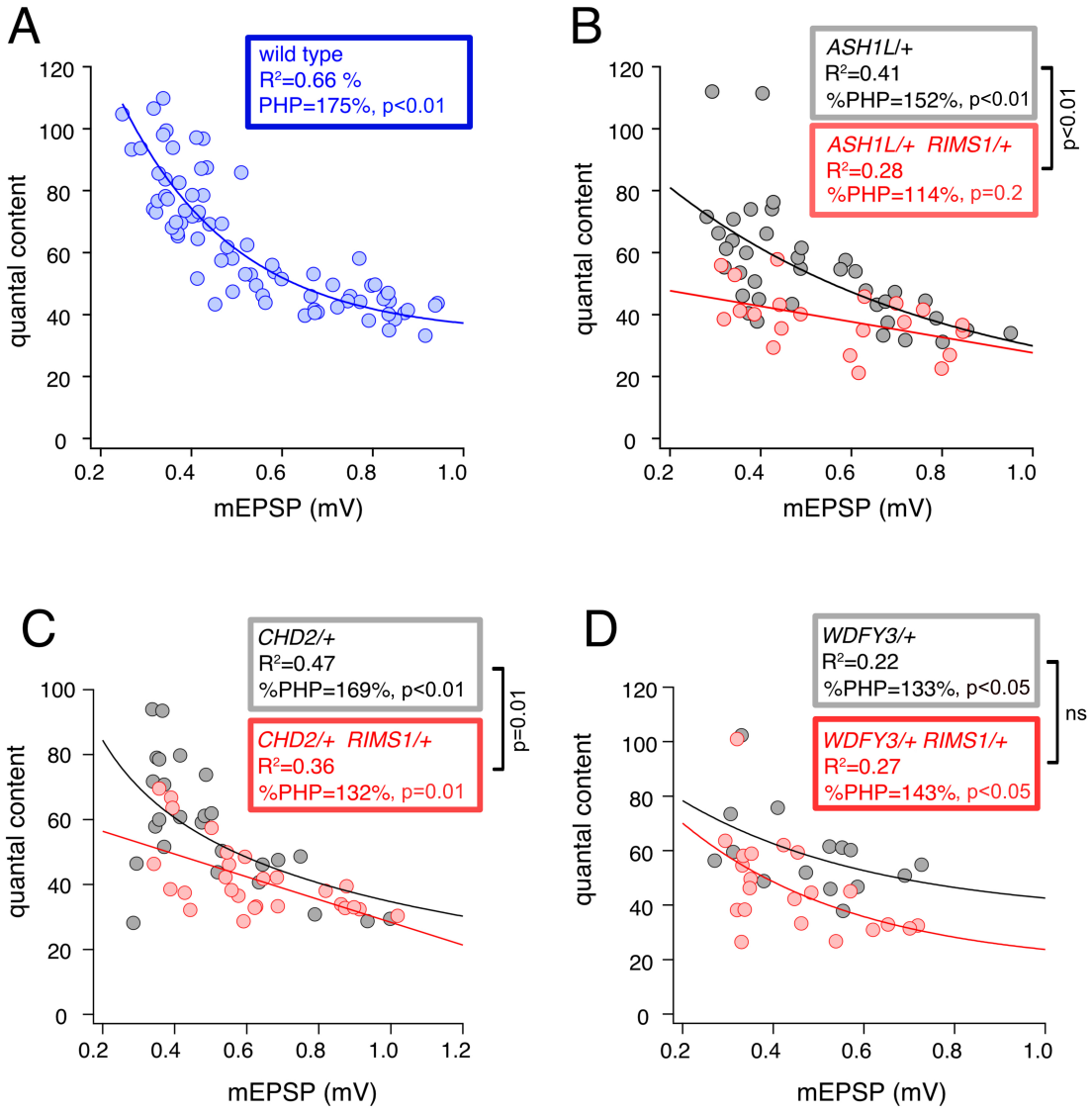

Figure S2: Double-heterozygous gene mutation combinations impair homeostatic plasticity. **A-D,** Scatter plots of quantal content (*y* axis) versus mEPSP amplitude (*x* axis) for **A,** *wild type*; **B,** *ASH1L/+, RIMS1/+* double heterozygous mutant (red) and *ASH1L*/+ heterozygous mutant (grey); **C,** *CHD2/+; RIMS1/+* double heterozygous mutant (red) and *CHD2*/+ heterozygous mutant (grey); **D,** *WDFY3/+; RIMS1/+* double heterozygous mutant (red) and *WDFY3/+* heterozygous mutant (grey). Each symbol represents an individual muscle recording. Exponential and line data fits (straight line, R^2-value inset). Boxes show statistics for curve fits and percent PHP expression (plus/minus PhTx). P-values within boxes report the statistical significance of PHP over genotypic baseline. P-values outside boxed compare PHP expression between genotypes.

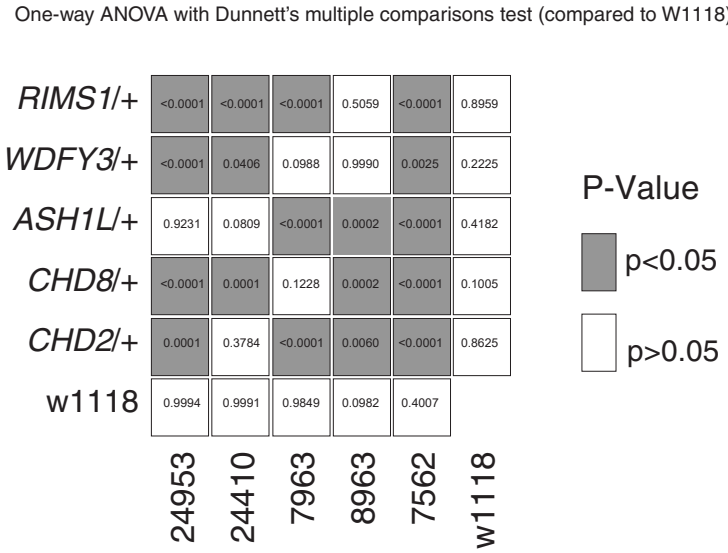

Figure S3: One-way ANOVA with Dunnett's multiple comparisons test (compared to *w188*) Genetic interaction matrix showing color-coded p-values from One-way ANOVA with Dunnett's multiple comparisons test. Each individual box represents p-values for the comparison of percent change in quantal content for a double-heterozygous mutant at intersection of x and y axes against wild type (*w1118*). Values are according to lookup codes at right (gray color indicates genotypes which have statistically significant difference, white color indicates no difference compared to w1118). **Note** that all comparisons indicated in gray are highly statistically significant with p<0.001, with the exception of two matrix element: *Df(24410)/+* with *WDFY3/+* is p=0.0406 and *Df(7562)/+* with *WDFY3/+* is p=0.0025.

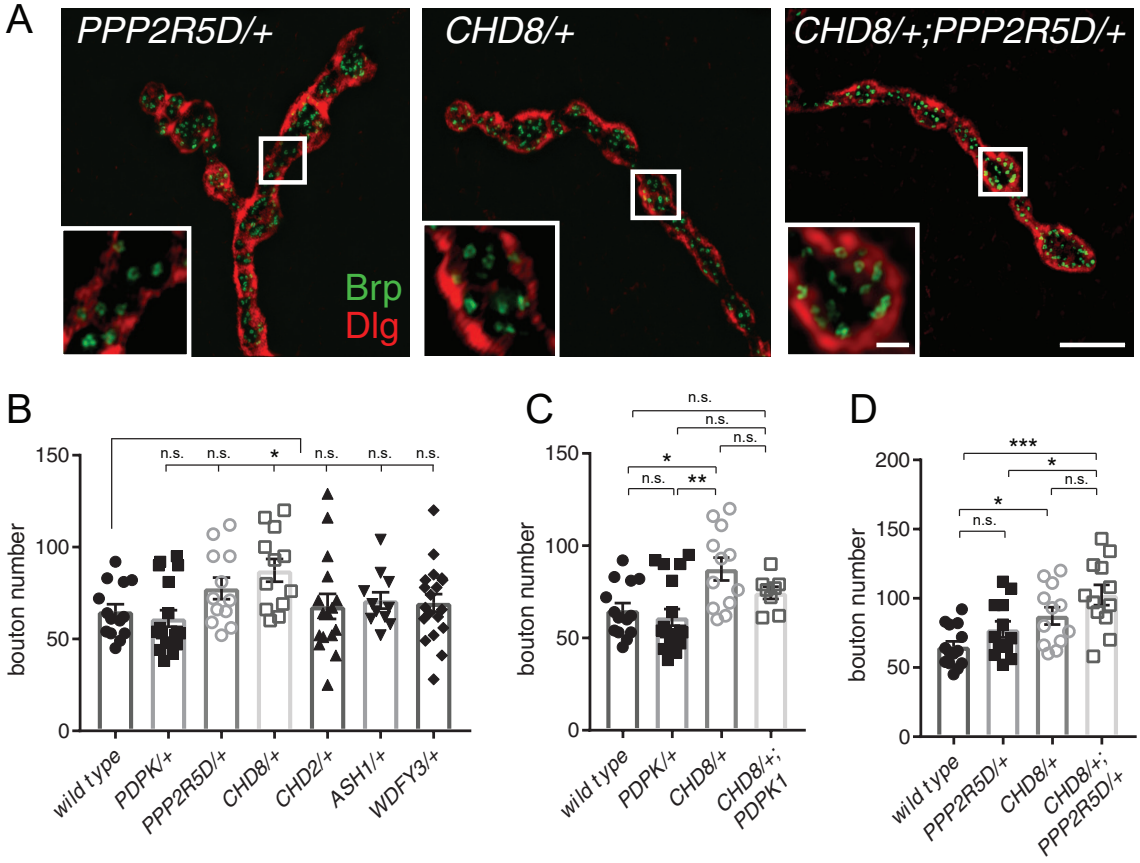

Figure S4: Analysis of the NMJ morphology

A, Structured illumination microscopy (SIM) images of neuromuscular junction for indicated genotypes. Insets show single confocal sections. Staining for anti-Brp (green) to mark active zones and anti-Dlg (red) to mark postsynaptic membranes. Scale bars: 5µm and 1µm (inset). **B,** Quantification of bouton number from NMJ (abdominal segments 2 and 3) for the indicated genotypes. One-way ANOVA, Dunnett's multiple comparisons, n.s $p>0.05$; * $p<0.05$ **C-D,** Data repeated from **(B)** highlighting specific comparisons for genotypes involving the heterozygous *CHD8/+* mutation. One-way ANOVA, Tukey's multiple comparisons, n.s $p>0.05$; * $p<0.05$; ** $p<0.01$; *** $p<0.001$. Data acquired and analyzed blind to genotype.

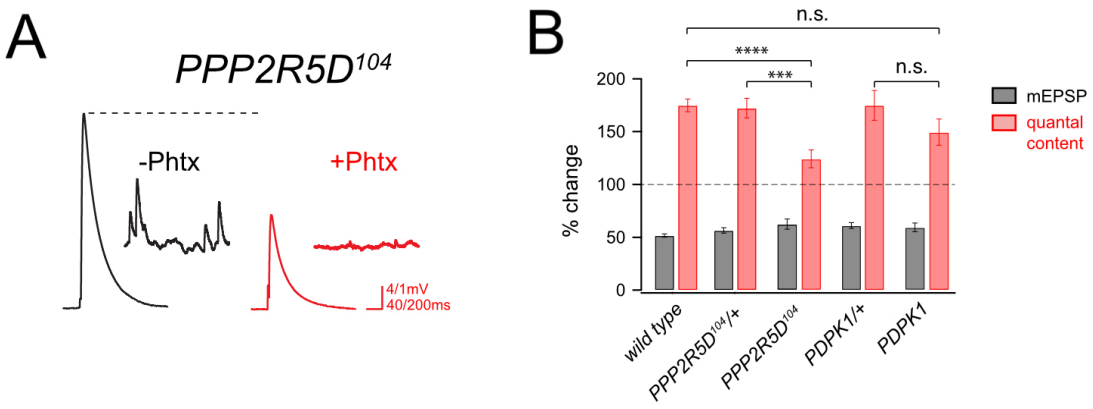

Figure S5: A *PPP2R5D* loss-of-function mutation disrupts PHP, but PDPK1 does not.
A, Representative mEPSP and EPSP traces for *PPP2R5D*^{104} homozygous mutant (-/+ PhTx) **B,** Percent change in mEPSP amplitude (gray bars) and quantal content (red bars) with PhTx compared to baseline for the indicated genotypes. Pairwise comparisons for each genotype (+/- PhTX), Student's t-test, two tailed; n.s. $p > 0.05$; *** $p < 0.001$; **** $p < 0.0001$.

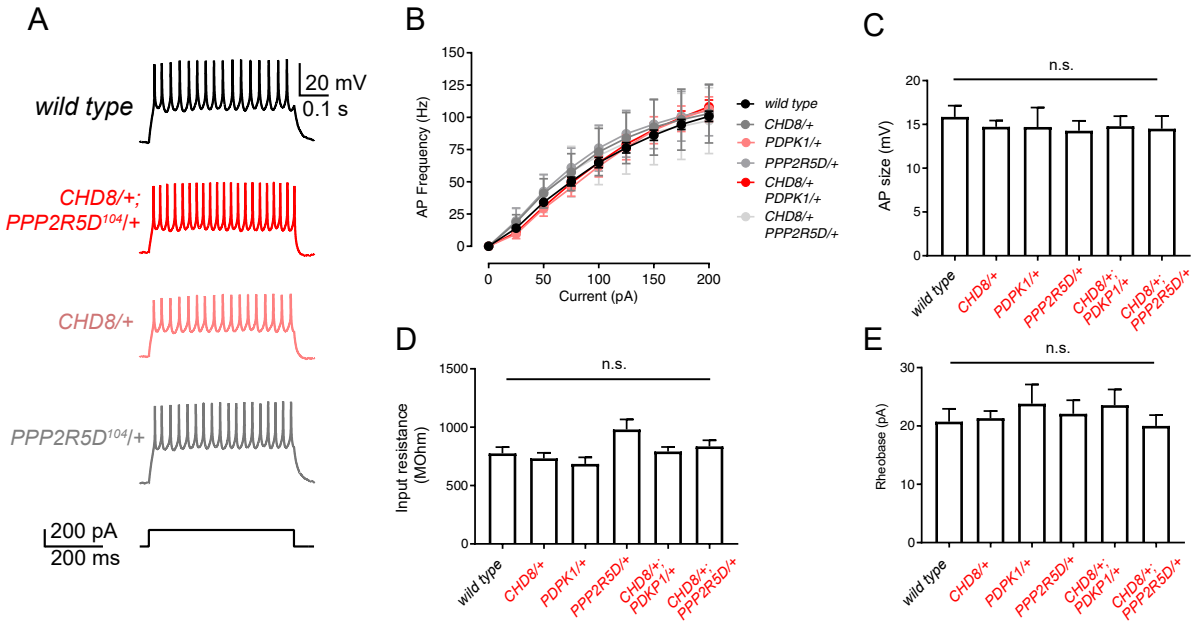

Figure S6: Firing properties of motoneurons are not different in a double heterozygous mutant
A, Representative traces for motoneuron firing upon injection of 200pA step current across indicated genotypes. **B**, Action potential frequency is plotted against current injection amplitude for wild type and mutant as indicated. **C-E,** Quantitation of action potential amplitudes, input resistance and rheobase for wild type and indicated genotypes. One-way ANOVA and Tukey's multiple comparisons (n.s. statistically not different, p>0.05).

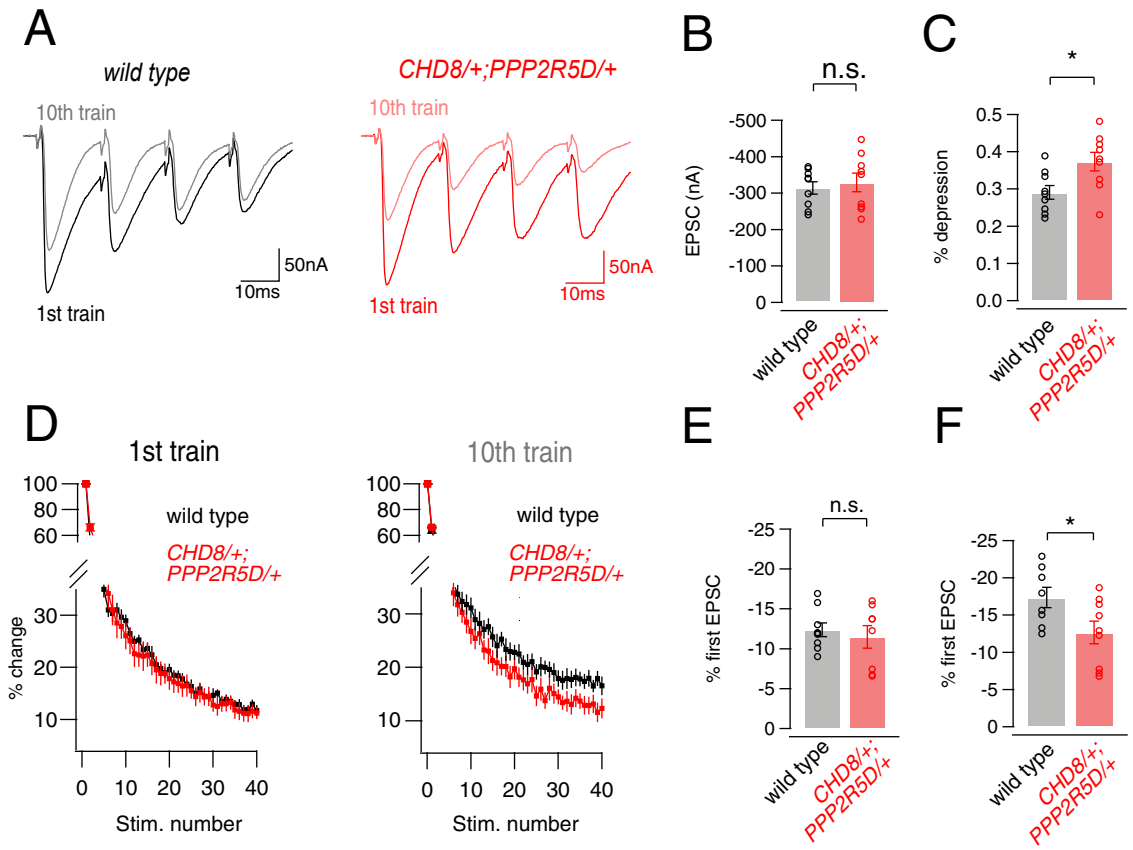

Figure S7: Analysis of short-term depression in *CHD8/+; PPP2R5D/+* double heterozygote
A, Representative traces for EPSCs following 50Hz stimulation (40 stimuli, 1st four shown for purposes of display) from *wild type* and the *CHD8/+;PPP2R5D/+* double heterozygous mutant. The first four EPSCs of the 1st and 10th trains are overlaid. **B**, Quantitation of first EPSC amplitudes. **C,** Percent depression of first EPSC comparing the 1st and 10th trains. **D,** Percent change (compared to first EPSC) for EPSC amplitudes during the train are plotted for wild type and double heterozygous mutant animal, as indicated. **E,** Quantification of the percent change in EPSC shown in **D** for the first train. **F,** percent depression of first EPSC after 10 trains. Student's t-test, two tailed; n.s. $p > 0.05$; * $p < 0.05$

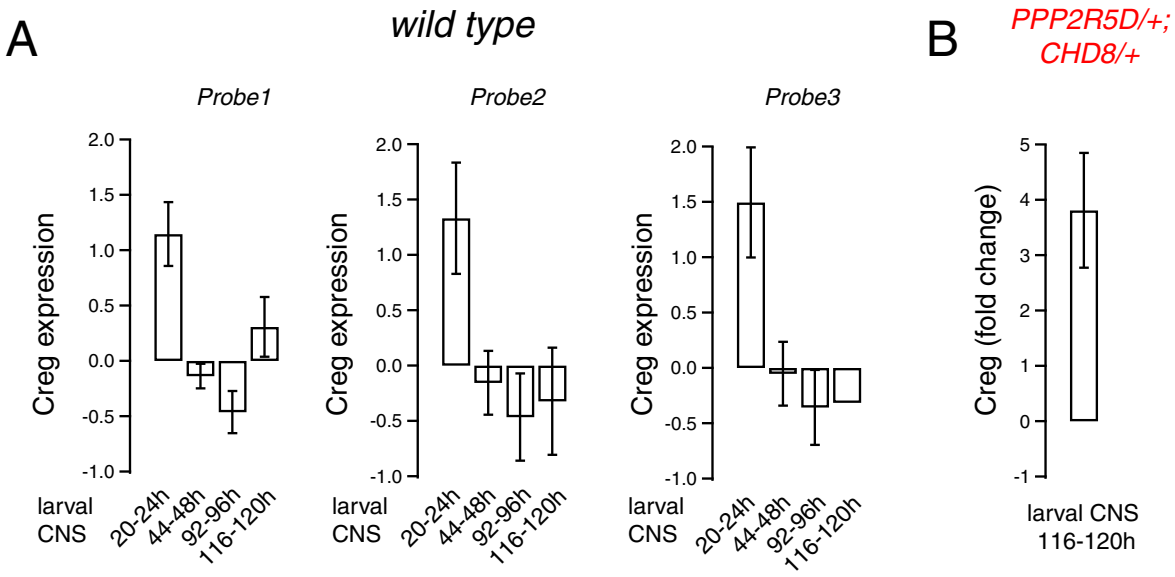

Figure S8: Expression levels of *CREG* during *Drosophila* larval development
A, CREG expression levels measured in larval CNS by microarray (log2) across different developmental time points with three different probes (see *57*). **B,** Quantification of CREG expression levels for the *CHD8/+; PPP2R5D/+* double mutant compared to *wild type* by qPCR (tissue source is larval CNS).

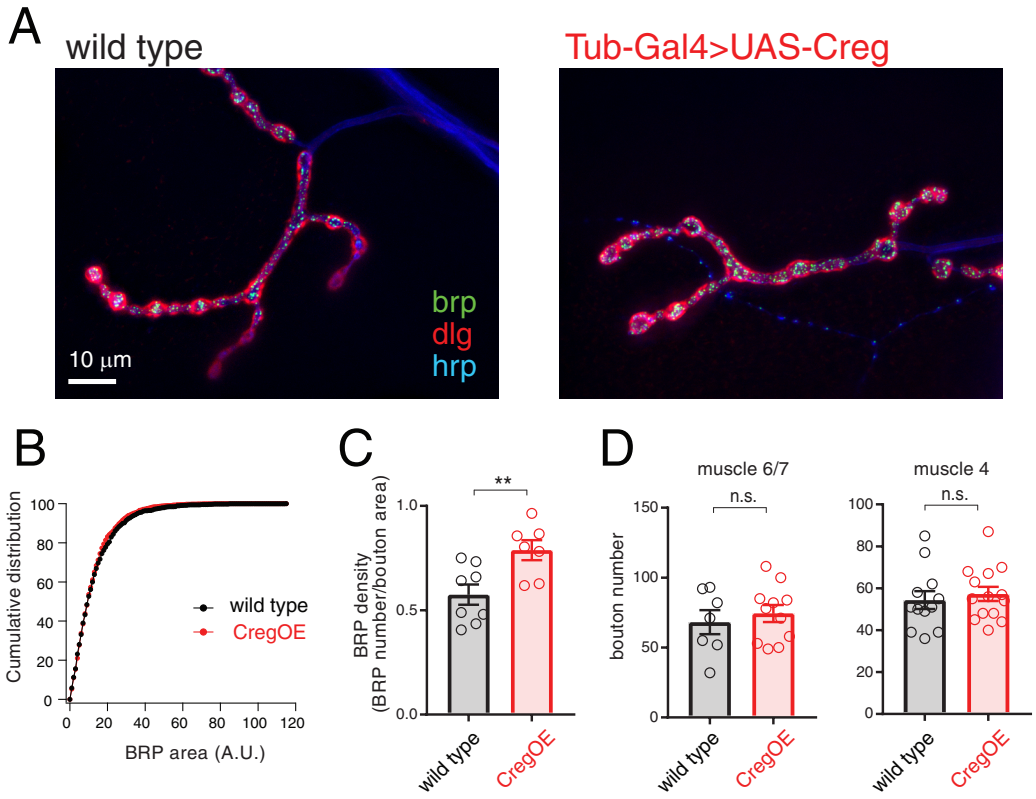

Figure S9: CREG overexpression does not substantively alter NMJ anatomy.
A, Immunostaining of *wild type* (left) and *Tub-Gal4>UAS-Creg* (right; CregOE) larval NMJ for Brp, DLG and HRP as indicated. **B,** Cumulative distribution plot of BRP area for *wild type* (black) and CregOE. **C,** Quantification of BRP density calculated by dividing the number of BRP positive puncta to the number of boutons. **D,** Quantification of bouton numbers in muscle 6/7 (left) and muscle 4 (right) for the wild type (black) and CregOE (red). Student's t-test, two tailed; n.s. $p > 0.05$; ** $p < 0.01$

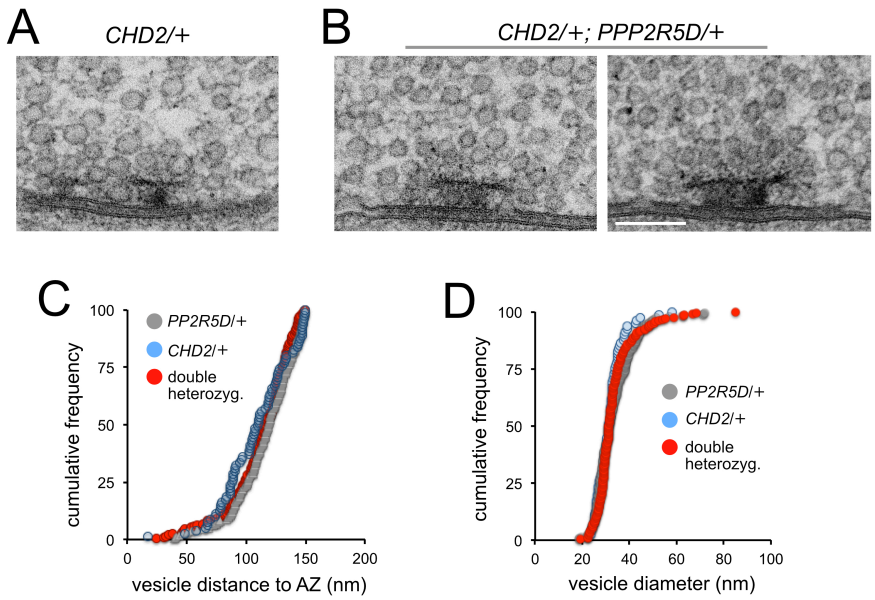

Figure S10: Ultrastructure analysis of the *CHD2/+; PDPK1/+* double heterozygous mutant. **A,** Representative example of the *CHD2/+* single heterozygous mutant NMJ. **B**, Two representative examples of the double heterozygous mutant. The membranes of the synaptic cleft are clearly defined as are clusters of synaptic vesicles of typical morphology and the electron dense T-bar structures. **C,** Quantification of vesicle distance to the active zone for all vesicles within 150nm radius of the T-bar centroid. **D,** Quantification of the distribution of synaptic vesicle sizes for the indicated genotypes.

Table S1. Deficiencies used in primary forward genetic screen.

(Bloomington Stock ID)					
7562	7614	7681	7977	9538	24927
7564	7616	7682	7980	9607	24952
7565	7619	7692	7981	9608	25116
7567	7620	7694	7983	9697	25117
7571	7621	7731	7990	9700	25123
7572	7622	7734	7992	9701	25388
7574	7624	7737	7994	9720	25389
7576	7635	7742	7997	9721	25413
7577	7637	7743	8057	23148	25444
7578	7638	7746	8061	23315	25688
7580	7641	7921	8063	23674	25694
7584	7644	7922	8068	24138	26505
7585	7648	7927	8070	24140	26507
7586	7649	7929	8074	24342	26534
7588	7652	7930	8083	24343	26538
7589	7653	7937	8097	24344	26832
7591	7657	7938	8100	24387	26833
7594	7658	7947	8963	24392	26839
7595	7659	7951	8970	24393	27346
7596	7660	7952	8973	24409	27361
7600	7662	7953	8974	24410	27362
7601	7664	7957	8976	24414	27368
7602	7666	7958	9071	24415	27369
7609	7672	7959	9214	24417	27375
7610	7674	7961	9292	24909	27580
7611	7675	7963	9497	24920	27912
7612	7676	7975	9499	24921	28827
7613	7680	7976	9500	24926	29027

Table S2:
Average mEPSP, EPSP and quantal content values for the Figure 1 and Figure 4

Genotype	mEPSP (-/+PhTx)	P-value	EPSP (-/+PhTx)	P-Value	Quantal Content (-/+PhTx)	P-value	n (-PhTx)	n (+ PhTx)
w1118/+	0.77/ 0.40	4.07E-19	33.3 / 29.7	0.00275	44.14 / 77.1	4.38E-17	47	36
7562/+	0.76/ 0.41	2.21E-06	34.1 / 22.1	0.00114	44.8/ 57.5	0.09556	6	7
8963/+	0.81/ 0.37	4.26E-08	35.7 / 21.8	3.10E-07	44.2 / 58.9	0.00064	8	10
7963/+	0.84/ 0.34	1.36E-10	28.8 / 23.4	0.31996	35.2/ 68.3	0.00301	8	8
24410/+	0.81/ 0.34	1.63E-07	31.3 / 21.8	0.00434	39.5 / 65.3	0.00029	8	11
24953/+	0.80/ 0.41	4.71E-14	26.1/ 22.9	0.19476	33.2/ 56.1	6.10E-05	13	15
CHD2/+	0.85/ 0.4	0.000104	28.67/ 25.63	0.27	36.16 / 64.33	0.00003	8	19
CHD2/+;7562/+	0.69/ 0.37	1.02E-07	30.7 / 14.2	1.70E-05	44.6/ 38.0	0.19615	4	10
CHD2/+;8963/+	0.69/ 0.37	0.00015	26.8/ 17.4	0.00358	38.6 / 47.0	0.00919	7	11
CHD2/+;7963/+	0.68/ 0.43	0.025	27.4 / 15.8	0.0006	43.3/ 39.0	0.5305	7	8
CHD2/+;24410/+	0.96/ 0.44	0.00001	31.9 / 19.1	0.0098	32.8/ 45.1	0.122	8	7
CHD2/+;24953/+	0.93/ 0.48	0.00121	21.14 / 12.66	0.00282	23.9 / 26.3	0.56128	8	12
CHD8/+	0.61/ 0.41	0.00461	29.90 / 25.82	0.09814	51.3 / 66.3	0.04464	7	8
CHD8/+;7562/+	0.48/ 0.45	0.50201	23.76 / 21.60	0.3212	52.1 / 48.8	0.6747	8	10
CHD8/+;8963/+	0.78/ 0.46	0.00061	29.89 / 20.89	0.00306	38.8 / 46.6	0.02838	9	17
CHD8/+;7963/+	0.63/ 0.35	2.23E-06	23.76 / 18.74	0.00843	41.1 / 53.7	0.06365	8	11
CHD8/+;24410/+	0.65/ 0.33	0.00041	24.91 / 16.97	8.70E-05	39.0 / 44.4	0.21624	6	14
CHD8/+;24953/+	0.60/ 0.41	1.57E-06	21.50 / 16.61	0.01199	36.8 / 41.2	0.26813	16	16

WDFY3/+	0.578875/ 0.368429	0.00103	29.7445 / 24.8531	0.29837	51.3489 / 68.0381	0.05123	8	7
WDFY3/+;7562/+	0.670429/ 0.318	0.00269	25.0508 / 14.2743	0.00314	40.3664 / 44.5645	0.51348	7	8
WDFY3/+;8963/+	0.730111/ 0.430333	4.05E-07	30.0532 / 24.3018	0.13024	33.3252 / 54.1519	0.00977	7	7
WDFY3/+;7963/+	0.59445/ 0.46625	0.00126	27.4833 / 27.5498	0.982	45.8709 / 59.252	0.0209	8	11
WDFY3/+;24410/+	0.607125/ 0.403375	0.00138	24.0743 / 19.645	0.09596	40.0525 / 49.6069	0.10056	8	8
WDFY3/+;24953/+	0.64075/ 0.383667	1.06E-05	22.9389 / 10.849	0.00472	35.601 / 28.4719	0.21712	8	9
RIMS1/+	0.7256/ 0.403444	1.15E-11	27.4848 / 25.1122	0.02848	38.5025 / 64.3644	5.10E-09	20	30
RIMS1/+,7562/+	0.670143/ 0.407667	0.00092	18.5703 / 12.6346	0.00521	27.8658 / 31.3246	0.16438	7	18
RIMS1/+,8963/+	0.730111/ 0.430333	0.01022	15.95 / 13.3405	0.26477	22.5791 / 31.1187	0.05777	6	9
RIMS1/+,7963/+	0.6035/ 0.350625	0.00782	25.9351 / 11.352	0.00105	43.0961 / 32.0142	0.00384	4	8
RIMS1/+,24410/+	0.634/ 0.336	2.54E-07	20.6415 / 13.2483	0.00619	33.148 / 41.1368	0.3635	7	13
RIMS1/+,24953/+	0.609333/ 0.402143	2.32E-05	19.3639 / 12.3295	0.0025	31.7789 / 28.4743	0.32924	6	7
ASH1L/+	0.749/ 0.39192	7.31E-08	29.3273 / 23.7862	0.00382	40.3736 / 61.5267	3.90E-05	15	25
ASH1L/+,7562/+	0.782636/ 0.368375	5.94E-05	24.9885 / 16.1292	0.00438	38.4814 / 43.5588	0.4614	11	16
ASH1L/+,8963/+	0.95325/ 0.42775	0.00209	23.7344 / 26.0928	0.49558	24.6505 / 61.5039	1.40E-05	8	8
ASH1L/+,7963/+	0.630455/ 0.405792	0.00087	30.649 / 17.4671	3.80E-05	50.8324 / 43.6606	0.21246	24	11
ASH1L/+,24410/+	0.7615/ 0.3755	5.55E-05	27.9698 / 19.6792	0.00051	37.8419 / 53.2772	0.00321	18	10
ASH1L/+,24953/+	0.86725/ 0.414391	5.85E-17	16.0195 / 14.5205	0.53663	18.6462 / 35.4708	0.00084	23	16

1301 **Table S3: Average mEPSP, EPSP and quantal content values for the Figure 5**

Genotype	mEPSP (/+PhTx)	P-value	EPSP (/+PhTx)	P-Value	Quantal Content (/+PhTx)	P-value	n -PhTx	n +PhTx
w1118/+; ; PPP2R5D/+	0.9224/ 0.5206	1.325E-11	30.4016375/ 29.22530625	0.63095	33.023/ 57.017	1.38E-06	8	16
PPP2R5D/+, RIMS1/+	0.7417/ 0.4137	1.1E-07	21.70959/ 15.1710092	3.69E-05	30.551/ 36.593	0.026631	20	25
CHD8/+; PPP2R5D/+	0.6489/ 0.3282	1.94E-08	27.09809091/ 14.483	1.95E-06	42.261/ 44.564	0.67508	11	14
CHD2/+; PPP2R5D/+	0.8533/ 0.4376	0.056815	35.991525/ 23.04841429	0.008342	44.365/ 52.739	0.202834	4	7
WDFY3/+; PPP2R5D/+	0.747/ 0.4671	4.23E-07	29.1565 / 16.776601	0.007575	39.171/ 35.781	0.589219	4	10
PPP2R5D/+, ASH1L/+	0.6745/ 0.4256	0.001933	23.14283333/ 22.3045	0.556417	35.942/ 53.071	0.001184	6	12
w1118/+; ; PDPK1/+	0.7028/ 0.4296	6.13E-07	26.683/ 28.143275	0.662673	37.838 / 66.343	0.000951	4	8
PDPK1/+, RIMS1/+	0.7768/ 0.41872	0.00033	26.40326/ 14.0144096	1.39E-06	36.797/ 33.149	0.442418	10	25
CHD8/+; PDPK1/+	0.7143/ 0.4258	0.090174	24.1224/ 19.8456	0.126857	35.584/ 47.375	0.054873	6	8
CHD2/+; PDPK1/+	0.7285/ 0.4461	2.9E-07	31.013825/ 20.7110125	4.55E-07	42.250/ 48.546	0.059572	4	8
WDFY3/+; PDPK1/+	0.7484/ 0.4719	0.000353	28.59798182/ 18.60855556	0.798318	38.963/ 42.250	0.001878	11	18
PDPK1/+, ASH1L/+	0.8828/ 0.5369	0.000442	23.16445 / 23.87097778	0.064927	28.049/ 45.030	0.277976	12	9